Applied Thermal Engineering 284 (2026) 129130

Contents lists available at ScienceDirect

Applied Thermal Engineering

journal homepage: www.elsevier.com/locate/apthermeng

Research Paper

Performance and cavitation in automotive centrifugal pumps: experimental analysis and 3D-CFD modelling assessment

Ilario Cordisco [a,*], Fabio Berni [a], Giovanni Paini [b], Roberto Tonelli [b], Stefano Fontanesi [a]

[a] Engineering Department "Enzo Ferrari", University of Modena and Reggio Emilia, Via Vivarelli 10, 41125 Modena, Italy
[b] Ferrari S.p.A., Via Abetone Inferiore 4, 41053 Maranello, MO, Italy

ARTICLE INFO

Keywords:
Centrifugal pump
Cavitation
CFD
Experiments

ABSTRACT

Centrifugal pumps are challenging components in several applications, including automotive cooling systems, where compact design, high efficiency and cavitation resistance are essential. This study develops and validates a predictive 3D-CFD methodology for the estimation of both performance and cavitation in complex-geometry centrifugal pumps adopted in high-performance vehicles. Two single-stage, single-suction pumps with comparable dimensions but distinct designs are investigated through a combination of experiments and CFD analyses. Experimental results are analysed using dimensionless coefficients, introducing a novel Performance Factor (PF) based on turbomachinery similitude to correlate cavitation onset with flow coefficient (φ) and cavitation number (σ). Pump X starts to exhibit cavitation for $\sigma < 0.5$ at $\varphi = 0.20$ and for $\sigma < 1.2$ at $\varphi = 0.34$. Pump Y shows cavitation at higher fluid temperature for $\sigma < 0.8$ and $0.21 < \varphi < 0.24$. As for the simulations, they compare three turbulence models (Realizable k-ε, k-ω SST, and Elliptic Blending Reynolds Stress Transport) and three rotational modelling approaches (frozen rotor, mixing plane, and sliding mesh), combined with the Schnerr-Sauer cavitation model. Quantitative comparison with the experimental data demonstrates that the k-ω SST turbulence model provides the best trade-off between accuracy and computational cost, with an average deviation of 4.3 % for pump X and 3.0 % for pump Y in predicting performance. The Elliptic Blending RST model reduces the deviation to 2.9 % but increases computational time by 70 %, limiting its practical use. Among the rotational models, the sliding mesh approach achieves the highest accuracy (4.3 % and 3.0 % deviation for pumps X and Y, respectively), while steady approaches (frozen rotor and mixing plane) show deviations up to 12.2 %, especially in off-design conditions. In cavitating regimes, sliding mesh and k-ω SST accurately capture the head losses, whereas alternative combinations significantly underestimate them. Additionally, mesh sensitivity analyses reveal that cavitating conditions require finer meshes than non-cavitating ones to accurately predict vapor formation. The adopted CFD framework thus provides a validated, computationally efficient, and predictive tool for the design and optimization of compact centrifugal pumps in automotive and other high-performance thermal management applications.

1. Introduction

Centrifugal pumps are driven turbomachines adopted in a vast range of applications. Examples include, but are not limited to, water supply to residential areas, irrigation [1], oil and gas industry [2,3], slurry transportation [4], desalination and power plants processes [5]. Centrifugal pumps can also be used as turbines (PAT) for energy recovery in various systems, demonstrating their versatility [6]. For what concerns the road transportation, centrifugal pumps are usually present in vehicles for engine cooling [7,8], and they also play a significative role for hybrid, electric and hydrogen vehicles, where the need to control the operating temperature of batteries, electric motor/generator, electronic devices and fuel cells [9] is of paramount importance.

Given the applications described above, it is straightforward to conclude that a careful design of pumps is necessary, to ensure high performance and avoid reliability issues due, for example, to the onset of cavitation. This last phenomenon not only poses a serious risk of mechanical damage but also degrades turbomachine performance even when no physical erosion occurs. The collapse of cavitation bubbles generates micro-jets and shockwaves that can erode the impeller surface and compromise the structural integrity of the pump, leading even to

* Corresponding author.
E-mail addresses: ilario.cordisco@unimore.it (I. Cordisco), fabio.berni@unimore.it (F. Berni), giovanni.paini@ferrari.com (G. Paini), roberto.tonelli@ferrari.com (R. Tonelli), stefano.fontanesi@unimore.it (S. Fontanesi).

https://doi.org/10.1016/j.applthermaleng.2025.129130
Received 23 August 2025; Received in revised form 26 October 2025; Accepted 11 November 2025
Available online 13 November 2025

Nomenclature

Symbols

A	Area [m^2]
N	Specific speed
PF	Performance factor
p_S	Static pressure [Pa]
p_T	Total pressure [Pa]
p_V	Fluid saturation pressure [Pa]
Q	Flow rate [l/min]
R_1	Radius of the impeller leading edges [m]
R_2	Radius of the impeller trailing edges [m]
Re	Reynolds number
T	Fluid temperature [°C]
v	Fluid velocity [m/s]
Δp_S	Static pressure rise [Pa]
Δp_T	Total pressure rise [Pa]
η	Hydraulic efficiency
ρ	Fluid density [kg/m^3]
σ	Cavitation number
τ	Torque [Nm]
φ	Flow coefficient
ψ	Head coefficient
ω	Rotational velocity [rad/s]

Subscripts

1	Inlet
2	Outlet

Acronyms

CFD	Computational Fluid Dynamics
CN	Cavitation number
DES	Detached Eddy Simulation
EXP	Experimental data
FC	Flow coefficient
HC	Head coefficient
LES	Large Eddy Simulation
MRF	Moving Reference Frame
NPSH	Net Positive Suction Head
PANS	Partially-Averaged Navier-Stokes
PAT	Pump As Turbine
RANS	Reynolds-Averaged Navier-Stokes
RNG	Re-Normalization Group
SST	Shear Stress Transport
URANS	Unsteady Reynolds-Averaged Navier-Stokes
VOF	Volume of Fluid
ZGB	Zwart-Gerber-Belamri

failure. In a cooling circuit, detached impeller fragments can further damage other system components, while reduced pump performance may either increase the power required to circulate the fluid or decrease the coolant flow rate, potentially leading to overheating.

Apart from experimental testing, which is cost- and time-consuming, Computational Fluid Dynamics (CFD) can be proficiently adopted at the preliminary stage by designers, in order to predict performance and cavitation onset and, if necessary, correct/improve the machine drawing. Thanks to the coupling with optimization tools, CFD can be also employed to increase the efficiency, which is a key aspect in specific applications such as automotive. Therefore, the development of a predictive CFD methodology able to simulate compact and complex geometries of automotive centrifugal pumps operating on wide ranges of flow rates, rotational velocities and temperatures is crucial. A predictive methodology enables more robust and energy-efficient designs, thus enhancing both reliability and efficiency of automotive cooling systems.

In literature, several studies focused on CFD analyses of centrifugal pumps are available. A review of the most recent and noteworthy works is reported in the following, in order to show the main currently-employed simulation methodologies.

Liu et al. [10] study cavitation in a high-speed-aircraft fuel centrifugal pump by means of frozen rotor approach, k-ω SST turbulent model and the Zwart-Gerber-Belamri (ZGB) cavitation model. It is found out that high flow rates, especially above the design one, can easily trigger cavitation, and the tendency is slightly reinforced by increasing the fuel temperature.

Dehghan et al. [11] propose a new criterion to determine the onset of cavitation in centrifugal pumps and validate it through experimental tests and CFD simulations on five single-stage centrifugal pumps. The simulation methodology relies on frozen rotor approach and ZGB cavitation model. Different turbulence models are tested and the k-ω SST emerges as the most accurate one. The new cavitation criterion provides a definition of the Net Positive Suction Head required ($NPSH_{r,\eta}$) of a pump as corresponding to a 3 % drop of efficiency, instead of considering a total head loss ($NPSH_{r,Ht}$). In fact, Dehghan et al. find that $NPSH_{r,\eta}$ is higher than $NPSH_{r,Ht}$ for all the considered pumps in the study. In particular, a 3 % drop of the total head corresponds to a 6.04 % of efficiency drop on average, ranging from 4.79 % to 8.92 % depending on the specific case. Using $NPSH_{r,\eta}$ provides a safety margin with respect to $NPSH_{r,Ht}$, leading to a reduction of cavitation and energy consumption.

Song et al. [12] study the effects of pre-whirl and modified blade profile on both hydraulic performance and cavitation of a centrifugal pump by numerical simulations. The selected framework consists of frozen rotor approach, RNG k-ε turbulence model and ZGB cavitation model. It is found out that a positive pre-whirl angle improves the efficiency for off-design flow rates thanks to significantly reduced friction losses. Additionally, head coefficient, hydraulic efficiency and torque of the centrifugal pump are improved with the redesigned blade profile, while inception and critical cavitation numbers of the modified impeller are gradually decreased down to 45.7 % and 43.1 %, respectively.

Ramirez et al. [13] characterize cavitation in dredging centrifugal pumps. The operating parameters of a cutter type dredger, namely swing speed, dredging depth and inclination, impeller rpm, as well as the slurry characterization (for example in terms of density and velocity) are introduced to determine how they influence the operation. CFD simulations are carried out using a Eulerian-Lagrangian approach for multiphase flows, frozen rotor approach, RNG k-ε turbulence model and a cavitation model based on the Rayleigh-Plesset equation. As research output, multiple regressions showing the influence of each of the variables on the dredge pump cavitation are provided.

An unsteady multi-phase cavitation model is employed by Li G. et al. [14] to investigate mass transfer and cavitation behavior of centrifugal pumps under various conditions and customize a simulation methodology to obtain the optimal combination of impeller blade number, blade wrap angle and blade installation angle. The numerical setup involves a sliding mesh approach, the k-ω SST turbulence model and the Schnerr-Sauer cavitation model. It is found that seven blades, blade wrap angle of 120° and blade installation angle of 30° are the optimal parameters for the studied centrifugal pump.

Li X. et al. [15] study unsteady (periodic) pressure field and head drop caused by leading edge cavitation in a single stage centrifugal pump by means of CFD. Frozen rotor and sliding mesh simulations are carried out using k-ω SST turbulence model in combination with the Schnerr-Sauer cavitation model. The main cause of the head-drop is due to the impeller inability to transform the potential energy into pressure

in the case of vortex flow as the cavitation blocks the blade channel. Additionally, as for the leading-edge cavitation, the amplitude of the pressure fluctuation at the blade passing frequency increases with the pressure decreasing at the pump inlet.

Tao et al. [16] study, both experimentally and numerically, the cavitation behavior in the pump mode of a reversible pump-turbine. The SST-DES method is used to consider the turbulence effect, while cavitation is solved with the ZGB model and the sliding mesh approach is used for the stator-rotor interaction. The results show that the best range of inception cavitation numbers and the best range of critical cavitation numbers have no intersection. In fact, the lowest inception cavitation numbers are found for the design conditions, while the lowest critical cavitation numbers are obtained for part-load conditions.

Shao and Zhao [9] try to improve cavitation resistance and hydraulic efficiency of liquid hydrogen centrifugal pumps, by employing a genetic algorithm in MATLAB and applying seven impeller parameters as optimization variables. The numerical validation of the pump model is carried out with sliding mesh approach, k-ω SST turbulence model for non-cavitating conditions and RNG k-ε for cavitating ones, and a modified Zwart cavitation model. The results show that by reducing the angle of the blades, increasing the diameter of the impeller and adding an inducer, the cavitation performance of the pump can be improved, while the hydraulic loss can be reduced by appropriately reducing the impeller outlet diameter, in order to improve the head of the pump.

Wang et al. [17] investigate the irreversible energy loss caused by cavitation flow in centrifugal pumps employing the entropy production theory. The numerical framework relies on the sliding mesh approach, a PANS turbulent model and the ZGB cavitation model. The predicted results show that the entropy production is consistent with the energy loss, and the latter is large in the impeller. Furthermore, the distribution of entropy production and flow details in the impeller are analyzed. It is found that severe cavitation changes the flow field structure and the area distribution of maximum entropy production, which is located near the blade suction surface and at the impeller outlet. Moreover, cavitation enhances the turbulent velocity fluctuation in the impeller, which is the main responsible for the increase of total entropy production.

Li et al. [18] train a deep-learning model with a dataset of CFD and experimental data to characterize the multiphase flow inside a cavitating centrifugal pump. The CFD dataset is constructed employing the sliding mesh method, the k-ω SST turbulence model, and the Schnerr-Sauer cavitation model. The predictions obtained by the deep-learning method on cavitation and both pressure and velocity fields agree with CFD, but with reduced calculation time. It is necessary to point out that one thousand pump geometries are designed and simulated for the construction of the CFD dataset.

Zhang et al. [19] analyze the composition and variation characteristics of the hydraulic radial force on the impeller of a six-blade end suction centrifugal pump using a data-centric approach based on CFD datasets. Using a sliding mesh approach coupled with the k-ω SST turbulent model, the hydraulic radial force of the pump exhibits a periodic behavior with a dominant frequency corresponding to the blade passing frequency. Moreover, at the design flow rate, the force components show minimal fluctuations, while deviations from the design flow rate lead to increased fluctuations.

A. Nycz et al. [20] investigate the influence of gaps in impeller blades on the performance of a low specific speed centrifugal pump through experimental and numerical analyses. The CFD simulations are steady-state and rely on the frozen rotor technique, with turbulence modelled by the k-ω SST. Results show that impellers with gaps achieve higher efficiency, up to 4 %, compared to the reference design without gaps, and also higher maximum pump capacity.

Y. Nishi et al. [21] employ a multi-objective optimization design method to achieve performance improvement and radial thrust reduction for single-blade centrifugal pump impellers. The 3D-CFD unsteady analyses are based on sliding mesh and k-ω SST. The optimized impeller shows 3.5 % improvement in efficiency, 18.1 % improvement in head coefficient, and 17.1 % reduction in the root mean square of the radial thrust compared to the original impeller. The CFD results are confirmed by experimental validation.

O. Dumitrescu et al. [22] compare CFD predictions with experimental measurements for micropumps (39.7 mm of impeller diameter), with the goal of evaluating the accuracy of CFD methods in complex microscale geometries. The impeller includes labyrinth sealings on its outer case. A first analysis only focuses on the leakage zone close to the sealings, which is studied with different approaches to turbulence (steady-state RANS with Standard k-ε, k-ω SST, or Spalart-Allmaras, URANS with k-ω SST, and LES). In this case, the LES approach is adopted as reference and the Standard k-ε is the one providing the best agreement. The second part of the analysis considers the whole pump, where LES is unfeasible due to prohibitive computational cost. Therefore, steady-state RANS simulations are employed to carry out new sensitivities to different parameters and models. In particular, different turbulence models (Standard k-ε, RNG k-ε, k-ω SST and Explicit Algebraic Reynolds Stress Model), different level of inlet turbulence intensity, and different roughness values are considered. Again, the Standard k-ε is found to be the best turbulence model. However, a mismatch between CFD results and experimental data is observed, as simulations underestimate the outlet total pressure up to about 10.0 %.

T. Huang et al. [23] provide a comparative analysis of the energy loss mechanisms in a multi-stage centrifugal pump operating in both turbine and pump modes. The CFD framework, validated against experimental data, consists in steady-state RANS simulations, where the k-ω SST turbulence model is employed, and the rotation of the impeller is considered through the frozen rotor technique. Results demonstrate that in both modes, turbulent entropy generation and wall entropy generation represent 54 % and 37 % of the total entropy generation, respectively. In turbine mode, the primary loss stems from the mismatch between the flow angle and the blade angle at the impeller inlet, while in pump mode the dominant losses are caused by the flow separation and the jet-wake structure within the flow channels.

In the light of the proposed literature review, it is possible to conclude that different models are available for the simulation of the different phenomena occurring during the operation of a centrifugal pump, but there is no consensus on a unique best practice. As resumed in Table 1, multiple approaches, regarding the modelling of impeller rotation, turbulence, and cavitation, are satisfactorily adopted in previous works. The rotor–stator interaction is handled via frozen rotor or sliding mesh methods. Turbulence is commonly treated with k-ω SST, though RNG k-ε, Standard k-ε, PANS, or DES are also used. Cavitation is simulated with Zwart-Gerber-Belamri, Schnerr-Sauer, or Rayleigh-Plesset models. These studies show that CFD can reliably predict cavitation onset, evaluate efficiency and head losses, investigate unsteady effects, optimize impeller geometry, and quantify energy loss mechanisms, but the optimal combination of models depends on the specific application. This work analyzes two water centrifugal pumps adopted in high-performance automotive cooling systems, with the aim of developing a reliable 3D-CFD modeling framework for investigating both hydraulic performance and cavitation in this context. Considering the variety of CFD choices (Table 1), this study evaluates and compares different rotational approaches (frozen rotor, mixing plane, and sliding mesh) and turbulence models (k-ε Realizable, k-ω SST, and Reynolds Stress Transport Elliptic Blending) to identify a best practice. Cavitation is examined using Volume of Fluid (VOF) method and the Schnerr-Sauer cavitation model. Although many cavitation models are available and currently used in literature, a deeper analysis on the effect of the cavitation model is not performed as the core of this study lies in the evaluation of rotational approaches and turbulence models. The numerical framework is validated against experimental tests on the pumps. Test data are handled with a dedicated post-processing technique, based on the definition of an original Performance Factor (PF), to extract data beyond their original aim. The proposed data analysis technique and numerical framework can be used to investigate centrifugal pumps for

Table 1
Review of the numerical methods employed in literature for the simulation of centrifugal pumps.

Authors	Publication year	Rotational approach	Turbulence model	Cavitation model
A. A. Dehghan, M. H. Shojaeefard, and M. Roshanaei [11]	2024	Frozen rotor	k-ε Standard k-ε Realizable k-ε RNG k-ω Standard k-ω SST	Zwart-Gerber-Belamri (ZGB)
O. Dumitrescu, C. Dobromirescu, V. Dragan, I. S. Vintila, and R. Mihalache [22]	2025	Frozen rotor	k-ε Standard k-ε RNG k-ω SST EARSM	–
T. Huang, T. Wang, Q. Guo, P. Shu, and Q. Gou [23]	2025	Frozen rotor	k-ω SST	–
G. Li et al. [14]	2022	Sliding mesh	k-ω SST	Schnerr-Sauer
G. Li et al. [18]	2024	Sliding mesh	k-ω SST	Schnerr-Sauer
X. Li, S. Yuan, Z. Pan, J. Yuan, and Y. Fu [15]	2013	Frozen rotor Sliding mesh	k-ω SST	Schnerr-Sauer
Q. Liu et al. [10]	2024	Frozen rotor	k-ω SST	Zwart-Gerber-Belamri (ZGB)
Y. Nishi, K. Konno, and S. Ono [21]	2025	Sliding mesh	k-ω SST	–
A. Nycz, J. Skrzypacz, and P. Szulc [20]	2025	Frozen rotor	k-ω SST	–
R. Ramirez, E. Avila, L. Lopez, A. Bula, and J. Duarte Forero [13]	2020	Frozen rotor	k-ε RNG	Modified Rayleigh-Plesset equation
X. Shao and W. Zhao [9]	2024	Sliding mesh	k-ε Standard k-ε RNG k-ω Standard k-ω SST	Modified Zwart model
P. Song, Z. Wei, H. Zhen, M. Liu, and J. Ren [12]	2022	Frozen rotor	k-ε RNG	Zwart-Gerber-Belamri (ZGB)
R. Tao, R. Xiao, F. Wang, and W. Liu [16]	2018	Sliding mesh	SST-DES	Zwart-Gerber-Belamri (ZGB)
X. Wang, Y. Wang, H. Liu, Y. Xiao, L. Jiang, and M. Li [17]	2023	Sliding mesh	PANS	Zwart-Gerber-Belamri (ZGB)
H. Zhang et al. [19]	2025	Sliding mesh	k-ω SST	–

automotive applications, in order to ensure improved efficiency and durability.

With respect to the existing works, there are four main elements of novelty in the present study. Firstly, the systematic comparison of different rotational approaches and turbulence models at both cavitating and non-cavitating conditions cannot be found elsewhere in literature. In this regard, mixing plane approach and Reynolds Stress Transport Elliptic Blending model were never tested before for pumps. Secondly, the targeted application, namely centrifugal pumps for automotive, lacks detailed exploration in the scientific literature. Such application is important as it strongly impacts the geometry and operating conditions of the machines. Indeed, as the pump must be accommodated within the limited space around the powertrain, its geometry becomes more intricate. Moreover, due to the transient and highly variable thermal loads in automotive cooling systems, the pump must reliably work over a broad spectrum of operating conditions. Thirdly, the proposed results point out a key-aspect, namely the grid-independence, which is strongly affected by the simulated conditions (cavitating or non-cavitating). Fourthly, a dedicated methodology for the post-processing of the experimental data is proposed. It makes it possible to obtain head loss curves for the validation of the CFD outcomes even if the experiments are not purposely carried out for that goal.

After the introduction, the experimental tests are presented and details on the numerical setup are given. Then, the results are proposed and commented and the main conclusions are drawn.

2. Experimental analysis

2.1. Experimental methods

The centrifugal pumps investigated in this study are single-stage, single-suction machines with semi-open impellers, to be employed in cooling circuits of high-performance engines. The working fluid is a 50 %–50 % water–glycol mixture (GlycoShell Longlife), representative of standard automotive coolant. Given their application in currently manufactured vehicles, the exact geometry of the pumps is confidential. However, their main features and dimensions are summarised below.

Although both pumps have similar overall dimensions typical of automotive applications, their internal designs substantially differ, thus remarkably affecting flow topology and simulation complexity. The inlet and outlet ducts are shaped to meet packaging constraints, resulting in geometries that are compact but hydrodynamically challenging.

Pump X features a straight, axial inflow duct with a diameter of 50 mm, directing the fluid along the impeller rotation axis and minimizing pre-swirl. The discharge duct includes a single functional bend redirecting the flow efficiently toward the system, while maintaining a compact design. The impeller has a diameter of 100 mm, seven blades and incorporates balancing holes, which reduce axial thrust and influence the internal flow distribution.

In contrast, Pump Y has a spiral-shaped inflow duct with the same initial diameter as pump X, introducing a controlled pre-rotation of the fluid before it enters the impeller. This affects the incidence angle on the blades and modifies the internal velocity distribution. The discharge duct features two functional bends, increasing the complexity of the flow path and enhancing the challenge for numerical modelling. The impeller has a diameter of 110 mm, eight blades, four balancing holes, and its shaft extends through both sides of the pump, strongly interacting with the incoming flow.

Overall, while the pumps share a similar compact scale, differences in inflow configuration, blade count, balancing features, and discharge duct geometry make them hydrodynamically distinct, providing a challenging test case for both experimental characterization and numerical simulation.

The experimental data are obtained from a closed-loop centrifugal pump test bench designed to evaluate hydraulic performance under controlled conditions. The facility consists of a main storage tank, which serves as a reservoir to supply and recirculate the test fluid while maintaining a nearly constant temperature, and a secondary buffer (nourice) tank located upstream of the pump inlet to stabilize suction conditions. The pump is coupled to an electric motor mounted on a rigid base. The motor is driven by a variable frequency drive (VFD), allowing control of the rotational velocity. The hydraulic circuit includes suction and discharge pipelines equipped with valves to regulate flow rate and discharge pressure. The system is instrumented with pressure transducers at the pump inlet and outlet, a flowmeter in the discharge line, and temperature sensors in the circuit to monitor fluid temperature. Further details can be found in Table 2. All sensors are connected to a data acquisition system that records the steady-state operating

Table 2
Working range and accuracy of the instruments used in the test bench.

Instrument	Working range	Accuracy
Siemens SITRANS FM MAG 5100 W	0 … 10 m/s	± 0.250 % (± 0.025 m/s)
WIKA S-10	0 … 10 bar	± 0.200 % (± 0.020 bar)
Endress + Hauser Omnigrad M TR10	− 50 … + 500 °C	± 0.016 % (± 0.100 °C)

parameters for each test point. During operation, the pump draws fluid from the buffer tank, discharges it through the measurement section, and returns it to the main tank, ensuring closed-loop circulation. Flow rate and head are adjusted using the discharge valve, and measurements are performed under stable conditions to obtain the characteristic curves of the pump.

Experimental tests are conducted with the aim to characterize the hydraulic performance of both pumps under controlled variations of inlet static pressure, rotational velocity, flow rate, and fluid temperature.

Before each test series, the circuit is filled with the 50 %-50 % water-glycol mixture used as coolant in current production engines and thoroughly deaerated to eliminate air bubbles. The fluid temperature is then stabilized at the value prescribed by the thermal control unit of the main tank, and continuously monitored during the tests. Fluid properties for the tested temperatures are shown in Table 3.

For each operating condition, the rotational velocity of the pump is set using the variable frequency drive controlling the electric motor. The inlet static pressure is adjusted by regulating the valve connected to the nourice tank. The flow rate is progressively varied by throttling the discharge valve, covering the entire operational range from near shut-off to maximum design flow.

Once steady state conditions are verified by monitoring the stability of the signals, flow rate Q, inlet static pressure $p_{S,1}$, outlet static pressure $p_{S,2}$, fluid temperature T, and rotational velocity ω are acquired.

For pump X, the tests are conducted at a fixed fluid temperature of 95 °C, with three different inlet pressures, and in the typical range of rotational velocities and flow rates of a cooling system for high-performance vehicles (i.e. $0 < \omega < 10,000\ RPM$ and $0 < Q < 1000\ l/min$). This allows the generation of a detailed performance map suitable for system-level modelling and control development.

For pump Y, the same procedure is followed at two fluid temperatures (100 °C and 120 °C) and a constant inlet pressure. The range of rotational velocities is adapted for each temperature, with the maximum speed at 100 °C approximately 30 % higher than the one at 120 °C, in order to avoid excessive cavitation at elevated temperatures.

The main output of the experiments is the static pressure rise of the pump Δp_S, defined as in Eq. (1).

$$\Delta p_S = p_{S,2} - p_{S,1} \tag{1}$$

$p_{S,1}$ and $p_{S,2}$ are inlet and outlet static pressures, respectively.

The impeller transfers mechanical energy to the fluid, increasing its velocity, which is then transformed into pressure by the volute. The mechanical energy acquired by the fluid is better quantified using the total pressure rise Δp_T instead of the static pressure rise Δp_S, because the former also considers the kinetic energy of the fluid. Indeed, the analysed pumps have slight differences between inlet and outlet diameters, resulting in a non-negligible contribution of the kinetic component. The gravitational potential, instead, can be neglected. The total pressure rise is defined as in Eq. (2).

$$\Delta p_T = p_{T,2} - p_{T,1} \tag{2}$$

$p_{T,1}$ is the inlet total pressure and $p_{T,2}$ is the outlet one. They are linked to the static pressures as in Eqs. (3) and (4).

$$p_{T,1} = p_{S,1} + \frac{1}{2}\rho v_1^2 = p_{S,1} + \frac{1}{2}\rho\left(\frac{Q}{A_1}\right)^2 \tag{3}$$

$$p_{T,2} = p_{S,2} + \frac{1}{2}\rho v_2^2 = p_{S,2} + \frac{1}{2}\rho\left(\frac{Q}{A_2}\right)^2 \tag{4}$$

ρ is the fluid density, v is the average flow velocity, A is the cross-section area, and Q is the flow rate, with the subscript 1 referring to the inlet and 2 to the outlet.

Another fundamental parameter for a pump is the hydraulic efficiency η, defined as in Eq. (5), which is the ratio between the mechanical energy acquired by the fluid and the mechanical energy used to move the impeller.

$$\eta = \frac{Q\Delta p_T}{\tau\omega} \tag{5}$$

τ is the pump torque and ω is the rotational velocity.

For confidentiality reasons, the previous quantities are made dimensionless by their maximum value, for each different dataset. Therefore, it is useful to define relative flow rate Q_r, relative total pressure rise $\Delta p_{T,r}$ and relative efficiency η_r as in Eqs. (6)–(8), respectively.

$$Q_r = \frac{Q}{Q_{max}} \tag{6}$$

$$\Delta p_{T,r} = \frac{\Delta p_T}{\Delta p_{T,max}} \tag{7}$$

$$\eta_r = \frac{\eta}{\eta_{max}} \tag{8}$$

In order to use a consolidated framework, data are also presented by adopting the typical dimensionless parameters for turbomachinery, namely flow coefficient φ (FC), head coefficient ψ (HC), and cavitation number σ (CN) [24], defined as in Eqs. (9)–(11), respectively. The adoption of dimensionless parameters is useful as it emphasizes the effect of the similitude theory.

$$\psi = \frac{\Delta p_T}{\rho(R_2\omega)^2} \tag{9}$$

$$\varphi = \frac{Q}{A_2 R_2 \omega} \tag{10}$$

$$\sigma = \frac{p_{S,1} - p_V}{\frac{1}{2}\rho(R_1\omega)^2} \tag{11}$$

R_1 is the outer radius of the impeller leading edges, R_2 is the outer radius of the impeller trailing edges, and p_V is the vapor saturation pressure.

The head loss due to cavitation is expressed by means of a performance factor (PF), defined as the ratio between the head coefficient at a certain operating condition and the value that it would have without cavitation (i.e. for sufficiently high cavitation number but same flow coefficient). PF is defined as in Eq. (12) and a graphical representation is visible in Fig. 3.

Table 3
Properties of the 50%–50% water-glycol mixture for the tested fluid temperatures.

Temperature T	Density ρ	Dynamic viscosity μ	Saturation pressure p_V
95 °C	1023.6 kg/m^3	$8.369{\cdot}10^{-4}$ $Pa{\cdot}s$	61,703 Pa
100 °C	1019.7 kg/m^3	$8.163{\cdot}10^{-4}$ $Pa{\cdot}s$	74,075 Pa
120 °C	1003.4 kg/m^3	$7.289{\cdot}10^{-4}$ $Pa{\cdot}s$	145,227 Pa

$$PF(\varphi,\sigma)=\frac{\psi(\varphi,\sigma)}{\lim_{\sigma\to\infty}\psi(\varphi,\sigma)} \tag{12}$$

This parameter is of primary importance to analyse cavitation when working with a vast range of operating conditions, because it is able to filter out all other effects. Indeed, PF is equal to one in non-cavitating working conditions, and it is reduced as cavitation gets more severe. Nevertheless, this parameter does not account for the cavitation inception (i.e. the formation of the first vapor cavities inside the pump), because the latter is not directly linked to performance degradation.

In addition, different pumps can be compared by means of the specific speed N, which is defined as in Eq. (13).

$$N=\frac{\omega Q^{1/2}}{\left(\frac{\Delta p_T}{\rho}\right)^{3/4}} \tag{13}$$

Although the experimental setup is designed for high accuracy, all measured data are subject to uncertainty. By considering the instrumentation accuracies (Table 2), it is possible to estimate relative errors of about 1–1.5 % for total pressure rise, 0.6 % for flow coefficient, 1–2 % for head coefficient, and up to 3 % for cavitation number. The uncertainty in hydraulic efficiency is 2–3 %, mainly due to torque measurement.

2.2. Experimental results

2.2.1. Performance assessment

Pump X is tested for a fluid temperature of 95 °C and three different inlet pressures. The results are shown in Fig. 1(a), where each curve represents a test carried out by adjusting the flow rate and keeping rotational velocity and inlet pressure constant. When the velocity is low, as well as the relative total pressure rise, it can be noted that curves with same velocity and different inlet pressures overlap. On the contrary, when the velocity and relative total pressure rise are high, a lower inlet pressure leads to a reduction of the pressure rise. This behaviour can be explained by cavitation, which is more likely to happen for high rotational velocities and low inlet pressures.

Pump Y, instead, is tested for two fluid temperatures (100 °C and 120 °C) at the same inlet pressure, and the results are shown in Fig. 1(b). The range of tested rotational velocities is adjusted to avoid excessive cavitation at high temperatures. Therefore, the maximum speed at 100 °C is approximately 30 % higher than at 120 °C. Due to the higher velocities, the relative total pressure increase is generally larger at 100 °C than that at 120 °C. Since two pairs of curves in the temperature datasets share the same velocity, they can be used to understand the temperature effect on the pump. They are referred in Fig. 1(b) as "ω_1" (in red) and "ω_2" (in blue). In both pairs, it is evident that a higher temperature generally leads to an increase in pressure rise, up to 20 % more, due to a reduced viscosity of the fluid. However, the saturation pressure increases from 74,050 Pa at 100 °C to 145,227 Pa at 120 °C, making the pump more likely to experience cavitation. As a consequence, the pressure rise advantage of a higher fluid temperature is reduced when cavitation arises at high flow rates. This is the case of the last flow rate at "ω_2", where cavitation is so severe that the total pressure rise at 120 °C is lower than the counterpart at 100 °C.

If the Reynolds number Re associated with the flow is sufficiently high, and cavitation is absent, the affinity laws for turbomachinery are valid. Therefore, all the head curves which respect the aforementioned conditions (i.e. for a sufficiently high CN) overlap when expressed in terms of dimensionless parameters (i.e. FC and HC), as it is shown for both pumps in Fig. 2. At this point, average head coefficient curves for non-cavitating operating conditions can be extracted through a simple polynomial regression and used as a reference for the simulations and for the computation of the performance factor (PF).

It is important to clarify how a "sufficiently high" CN is defined. To explain that, it must be noted that a HC curve made by keeping rotational velocity, inlet pressure, and temperature constant (as it is done in the tests) is associated with only one CN. Indeed, for a given pump geometry, the CN depends only on inlet pressure, fluid properties (which depend on temperature) and rotational velocity as shown in Eq. (11). Therefore, by comparing HC curves associated with different values of CN, it is possible to define a threshold of CN beyond which the HC curve does not change anymore. This is the procedure adopted to obtain the HC curves presented in Fig. 2.

Pump X is slightly more compact and faster than pump Y, but the

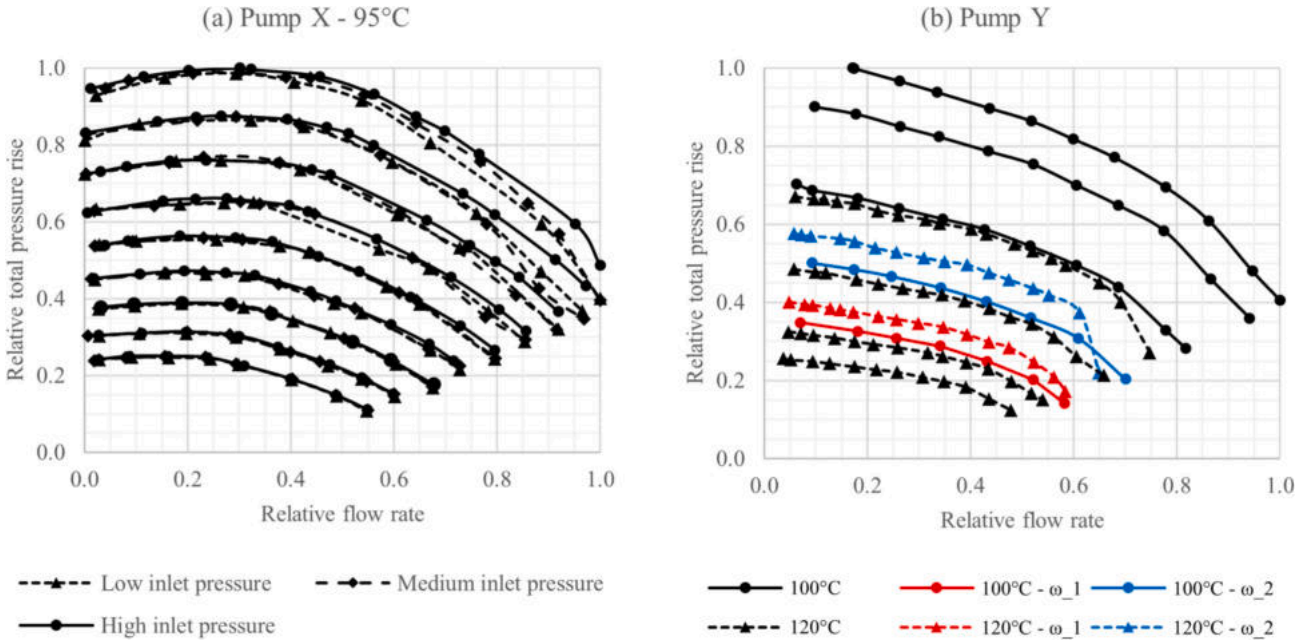

Fig. 1. Relative total pressure $\Delta p_{T,r}$ against relative flow rate Q_r for (a) pump X and (b) pump Y. Pump X is tested for three different inlet pressures, keeping the fluid temperature constant. Instead, pump Y is tested for two fluid temperatures, keeping the inlet pressure constant. The tested rotational velocities of pump Y differ for the two temperatures, but the red and blue curves are the only ones sharing the same velocities.

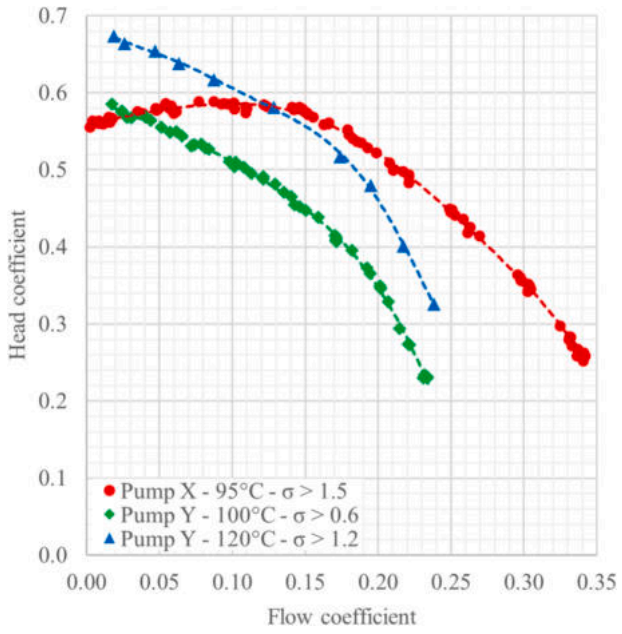

Fig. 2. Comparison in terms of head coefficient ψ, against flow coefficient φ, between pump X (95 °C) and pump Y (100 °C and 120 °C). The presented points are only those unaffected by cavitation (i.e. with a sufficiently high cavitation number σ).

difference is small because they are used for the same application. Indeed, both pumps share a similar design specific speed N of 0.5. Nevertheless, in non-cavitating conditions and with similar fluid temperatures, pump X has a higher HC compared to pump Y over the entire range of tested FCs, and it is able to work at higher FCs. Considering pump Y, it is easier to see the performance advantage of working at a higher temperature by comparing the HC curves at 100 °C and 120 °C.

For what concerns cavitation, pump X is unaffected by cavitation for a CN higher than 1.5, while pump Y is completely unaffected at 100 °C, and unaffected above CN equal to 1.2 at 120 °C.

Although pump X is more performant than pump Y, and working at higher temperatures improves head, pump Y is more resistant to cavitation, especially at low fluid temperatures.

To clarify the comparison between HC curves at different CNs, Fig. 3 shows all the points of a given dataset, coloured based on the associated CN.

In particular, Fig. 3(a) shows the dataset of pump X (95 °C). In this case, the machine presents operating points where the HC is clearly lower than the maximum value that other points can assume at the same FC. All the points that manifest such a behavior are associated with a low CN, making cavitation the most reasonable explanation for this phenomenon. Additionally, the hypothesis is enforced by the fact that the lower the CN is, the lower the HC becomes, as expected by cavitation. Similar considerations are also valid for pump Y, when the fluid temperature is 120 °C, as it is shown in Fig. 3(b). Conversely, operating pump Y with a fluid temperature of 100 °C does not cause this behaviour. Indeed, all points overlap into a single HC curve independently of the CN, as it is shown in Fig. 2.

Efficiency data are available only for pump X, and they are calculated by means of the torque on the pump shaft during the tests. Hence, they also consider the mechanical losses due to friction between parts, and not only the torque applied by the impeller to the fluid, which is measured by CFD simulations. Fig. 4 shows the efficiency results of pump X (95 °C) for different ranges of CN. The best efficiency point is located at a FC of 0.18, and 90 % of the peak value is obtained in the range $0.13 < \varphi < 0.25$. At the highest flow coefficient (0.34), the pump works at 60 % of its best efficiency. Additionally, low CNs and high FCs are associated with a reduction of efficiency, but the trend is not as clear as for HCs. HC and efficiency are strictly connected, but the latter is also affected by the torque applied to the impeller, which can add more uncertainty to the measure. Considering the availability of the data for only one pump, and the intrinsic difference (due to friction) between experimental and simulated torque, efficiency is not used for the validation of the CFD methodology. Nevertheless, it is useful to keep in mind that pump X is designed to work for a FC of 0.18, where the efficiency is maximum, and cavitation affects it for high FCs.

2.2.2. *Cavitation assessment*

Cavitation can be detected monitoring the head decrease of a pump when the inlet pressure is reduced, keeping all the other conditions constant. The datasets of this study were originally made to build performance maps of both pumps as part of engine cooling circuits.

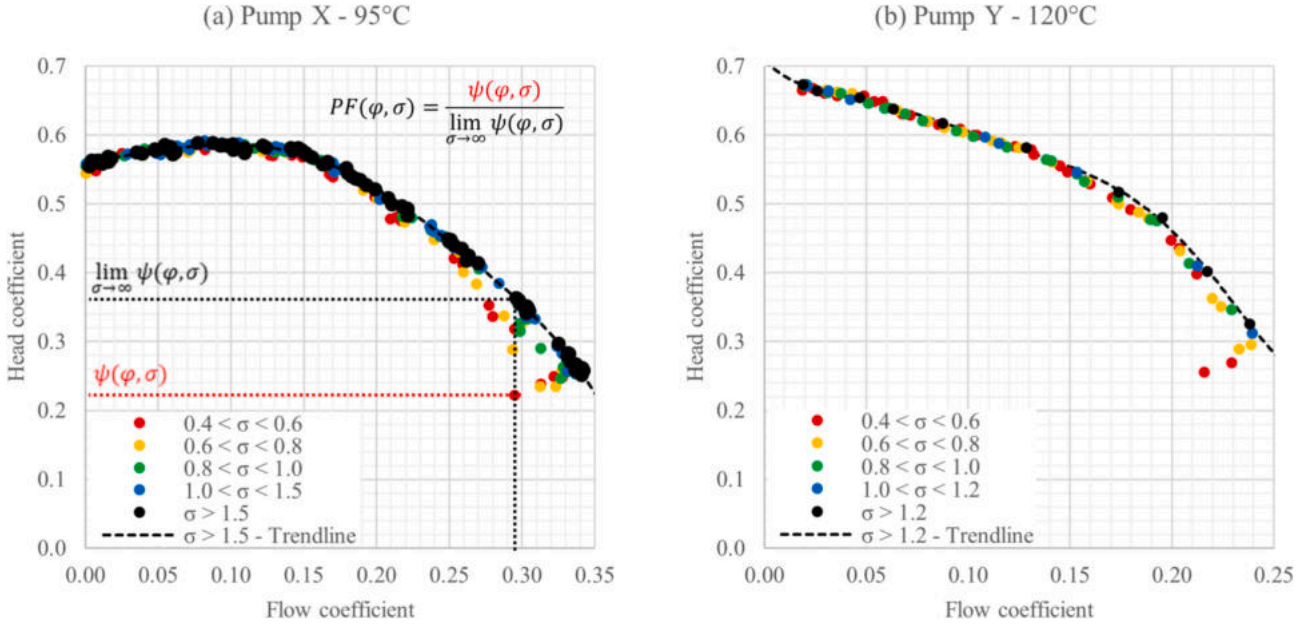

Fig. 3. Comparison in terms of head coefficient ψ between operating points at different cavitation numbers σ for (a) pump X and (b) pump Y. A graphical representation of the performance factor PF is also shown.

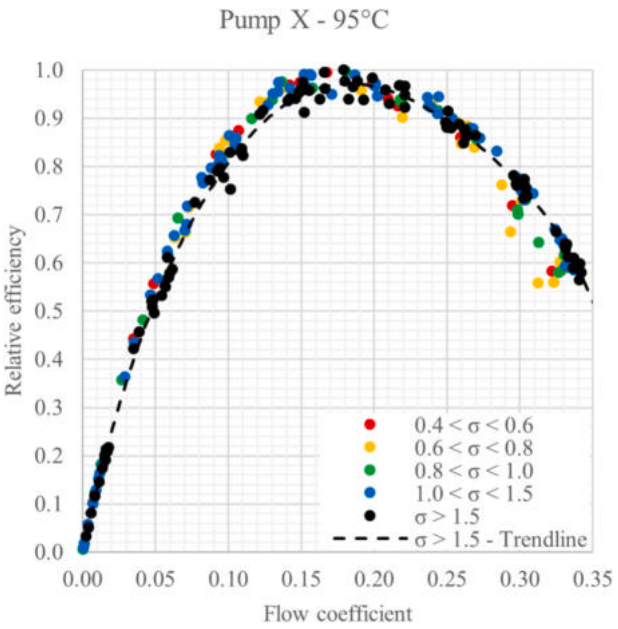

Fig. 4. Relative efficiency η_r against flow coefficient φ for pump X (95 °C).

Therefore, only few levels of inlet pressure are available, as possible operating conditions of the system. On the other hand, the number of tested velocities is high because both pumps are coupled to engines, which work on a wide velocity spectrum. Unlike stationary pumps, which work at nearly constant velocity and are optimized to avoid cavitation and be very efficient in a narrow range of flow conditions, automotive pumps are meant to operate in a large velocity range while the system pressure is usually stable. Therefore, given that the experimental tests are representative of automotive conditions, they are not able to provide the head loss curves (i.e. head as a function of inlet pressure) usually presented in literature. In different terms, the datasets do not present tests carried out by gradually reducing the inlet pressure while flow rate, rotational velocity, and temperature are kept constant, which is the standard procedure to address cavitation. Instead, inlet pressure is kept constant as the rotational velocity changes through the whole operating range. In this sense, the proposed experiments explore the effect of impeller velocity on cavitation more than that of inlet pressure.

When working with different inlet pressures, it is possible to show head loss curves without the need for dimensionless parameters as FC, HC, and CN. Instead, the rotational velocity of the impeller affects both head of the pump and its tendency to cavitation. Therefore, the turbomachinery affinity laws become necessary instruments to address the problem. In dimensionless terms, cavitation can be analysed by considering how much the HC drops when the CN is reduced, for a given value of FC. It is a common industrial practice to define the drop of pump head relatively to the value that it would have in absence of cavitation (i.e. at high inlet pressure for given rotational velocity and flow rate). Consequently, a certain percentage (usually from 3 to 5 %) of head loss is enough to identify severe cavitation of the pump. This is translated in dimensionless terms by considering the relative HC loss, which is called Performance Factor *PF* in this work, and it is defined in Eq. (12).

Fig. 5 shows the *PF* for every operating point of pump X (95 °C) and pump Y (120 °C) as a function of FC and CN. Pump X (95 °C) has points with a PF lower than 0.95, which denotes severe cavitation, for FCs over 0.2 and CNs below 1.2. In particular, increasing FC causes severe cavitation to start earlier, that is for higher CNs. Indeed, PFs below 0.95 can be seen at CN equal to 0.5 for a FC of 0.21, but at a much higher CN (namely 1.2) for the highest FCs. A similar behavior is also visible in pump Y (120 °C), where the PF falls below 0.95 for FCs above 0.21 and CNs below 0.8. Coming back to dimensional parameters, this means that both pumps are affected by cavitation when rotational velocity and flow rate are high.

Considering different ranges of PF, it is possible to notice that points with $0.95 < PF < 0.97$ mainly surround those with $PF < 0.95$. Instead, points with $0.97 < PF < 0.99$ show higher dispersion. Indeed, cavitation has a non-linear behavior, causing a slow reduction of HC for large ranges of CN, and then abruptly accelerating near the complete cavitation breakdown of the pump. In addition to this, it is useful to remember that the PF relies on average HC curves obtained for sufficiently high CNs, which are meant to represent non-cavitating conditions. Therefore, experimental uncertainty can play a significant role and has to be considered. As an example, pump X has many points with $0.97 < PF < 0.99$ for CN above 2.0. Such points do not have to be necessarily

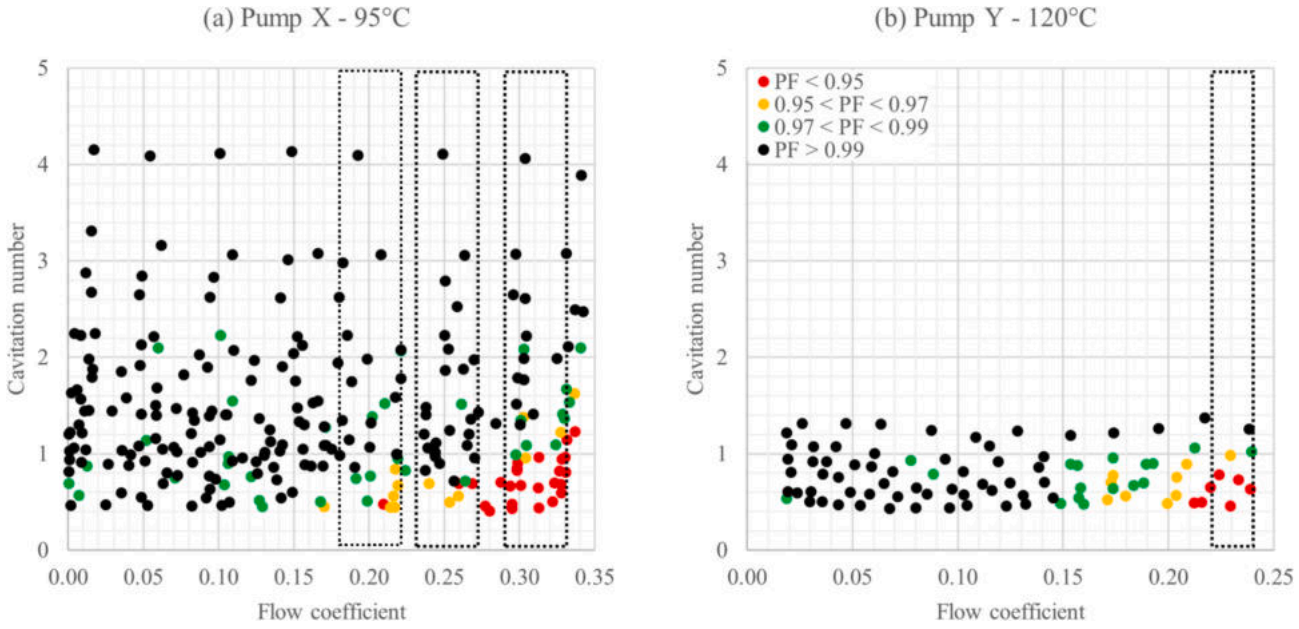

Fig. 5. Performance factor *PF* as a function of flow coefficient φ and cavitation number σ for (a) pump X and (b) pump Y. The boxes represent the flow coefficient ranges evaluated in this study.

associated with cavitation, because measuring uncertainties (regarding pressure, flow rate, and fluid temperature) may cause deviations higher than 1 % in the HC values.

Another advantage of the PF is the possibility to analyse a (small) range of FCs instead of a single value. In fact, a slight change of FC can substantially change the value of HC, making challenging to detect the effect of cavitation. Instead, PF can be modified only by cavitation, allowing for the analysis of a larger data sample. Therefore, in this study, four ranges of FC (i.e. $0.18 < \varphi < 0.22$, $0.23 < \varphi < 0.27$, and $0.29 < \varphi < 0.33$ for pump X, and $0.22 < \varphi < 0.24$ for pump Y) are selected for a more detailed analysis of cavitation and the validation of the CFD methodology.

Fig. 6 shows the PF as a function of the CN for the aforementioned FC ranges, and the experimental points are then fitted with an exponential regression. In details, the fitting curves have the formulation reported in Eq. (14).

$$PF_{Trendline}(\sigma) = 1 - Ae^{-B(\sigma - C)} \tag{14}$$

A, B and C are coefficients obtained by minimising the standard deviation with respect to the experimental data.

The first thing to notice is the relatively large dispersion of the experimental data, which is due to two main factors. The first one is the necessity of broadening the dataset by considering a (small) range of FCs instead of a single value. As it is shown in Fig. 5, cavitation is influenced by the FC. Indeed, pumps are designed to work for a particular FC, where the flow is regular and losses are minimised. So, when a pump operates far from its nominal FC, flow detachments or recirculation zones can appear, increasing the possibility of cavitating behaviour. Therefore, as the distance from the nominal FC increases, the head loss due to cavitation can appear for higher CNs. In this sense, it is expected that the PF can change inside a range of FCs, thus requiring the range to be small enough to filter out this effect, but large enough to include a relevant amount of data. The second factor regards the intrinsic approximation introduced by the theory of similarity laws, which adds dispersion to the data even in non-cavitating conditions. As a consequence, data fitting through a regression curve is a useful technique to capture the mean behaviour of cavitation for a given FC range.

The second thing to notice is that, despite data dispersion, both pumps show evident trends for what concerns the losses due to cavitation. In particular, thanks to the larger amount of data available for pump X, it is possible to compare three different PF curves, which correspond to the same number of FC ranges. It is evident that cavitation is more severe as the FC increases. Indeed, for both the ranges $0.18 < \varphi < 0.22$ and $0.23 < \varphi < 0.27$, the performance factor drops below 0.95 around a cavitation number of 0.5. Instead, cavitation is definitely more severe in the range $0.29 < \varphi < 0.31$, where there are points with PF below 0.95 as soon as the CN falls below 1.0.

Moving to pump Y, its cavitating behaviour is more sensitive to the FC compared to pump X, so the considered range of FCs has a width of 0.2, which is narrower than the 0.4 span of those used for pump X. As a consequence, fewer points are employed, but their trend is still a reliable indication of cavitation. In this case, the PF drops below 0.95 when the CN is lower than 0.8.

The trend lines proposed in Fig. 6 will be adopted in the following for the validation of the CFD setup under cavitating conditions.

3. Numerical analysis

3.1. Numerical methods

CFD simulations are carried out with the commercial software STAR-CCM+ [25], licensed by SIEMENS DISW. Turbulence is considered through a RANS approach, while the energy equation is not solved as the simulations are treated as isothermal. In the case of a single-phase physics, the governing equations are written as in Eqs. (15) and (16).

$$\frac{\partial \rho}{\partial t} + \frac{\partial}{\partial x_j}(\rho u_j) = 0 \tag{15}$$

$$\frac{\partial}{\partial t}(\rho u_j) + \frac{\partial}{\partial t}(\rho u_i u_j) = f_i - \frac{\partial p}{\partial x_i} + \frac{\partial}{\partial x_j}\left[(\mu + \mu_t)\left(\frac{\partial u_i}{\partial x_j} + \frac{\partial u_j}{\partial x_i} - \frac{2}{3}\delta_{ij}\frac{\partial u_k}{\partial x_k}\right)\right] \tag{16}$$

ρ is the fluid density, t is the time, x_i is the position in the i-th direction, u_i is the velocity component in the i-th direction, f_i is the specific body force in the i-th direction, p is the pressure, μ is the dynamic viscosity of the fluid, μ_t is the turbulent viscosity, and δ_{ij} is the Kronecker delta (i.e. $\delta_{ij} = 1$ if $i = j$, otherwise $\delta_{ij} = 0$).

In order to study the cavitation effects on performance, a multi-phase physics coupled with a cavitation model is required. In this study, the Volume of Fluid (VOF) method [26] and the Schnerr-Sauer cavitation

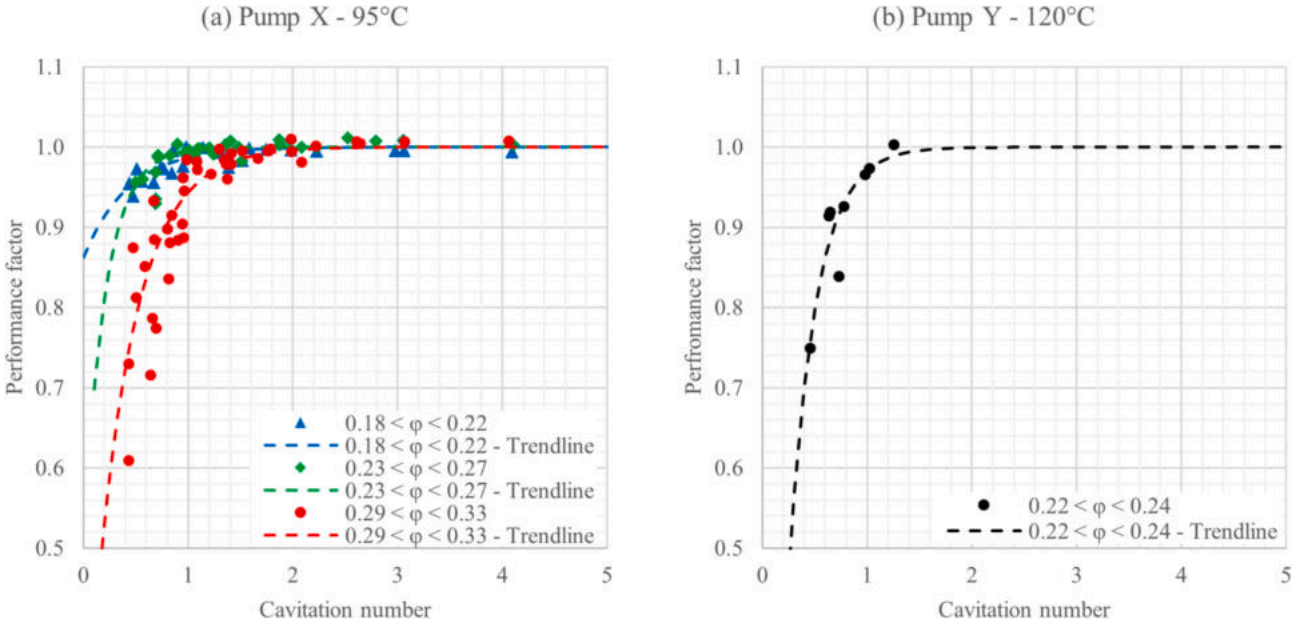

Fig. 6. Performance factor *PF* against cavitation number σ for different flow coefficient φ ranges (depicted in Fig. 5) of (a) pump X and (b) pump Y.

model [27] are adopted. Therefore, the governing equations are written as in Eqs. (17) and (18).

$$\frac{\partial \rho_m}{\partial t} + \frac{\partial}{\partial x_j}\left(\rho_m u_j\right) = 0 \tag{17}$$

$$\frac{\partial}{\partial t}\left(\rho_m u_j\right) + \frac{\partial}{\partial x_j}\left(\rho_m u_i u_j\right) = f_i - \frac{\partial p}{\partial x_i} + \frac{\partial}{\partial x_j}\left[\left(\mu_m + \mu_t\right)\left(\frac{\partial u_i}{\partial x_j} + \frac{\partial u_j}{\partial x_i} - \frac{2}{3}\delta_{ij}\frac{\partial u_k}{\partial x_k}\right)\right] \tag{18}$$

ρ_m is the mixture density and μ_m is the mixture viscosity, which are defined by the volume fractions of liquid (α_l) and vapor (α_v) as in Eqs. (19) and (20). The sum of α_l and α_v is equal to 1.

$$\rho_m = \alpha_l \rho_l + \alpha_v \rho_v \tag{19}$$

$$\mu_m = \alpha_l \mu_l + \alpha_v \mu_v \tag{20}$$

ρ_l is the liquid density, ρ_v is the vapor density, μ_l is the liquid dynamic viscosity, and μ_v is the vapor dynamic viscosity.

The VOF method requires an additional transport equation for the volume fraction of vapor α_v, which assumes the form of Eq. (21) by using the Schnerr-Sauer cavitation model.

$$\frac{\partial \alpha_v}{\partial t} + \frac{\partial(\alpha_v u_i)}{\partial x_i} = \left(\frac{n_0}{1 + \frac{4}{3}\pi R^3 n_0}\right)\frac{d}{dt}\left(\frac{4}{3}\pi R^3\right) = \left(\frac{4\pi R^2 n_0}{1 + \frac{4}{3}\pi R^3 n_0}\right)\dot{R} \tag{21}$$

n_0 is a user-defined parameter which represents the bubble concentration per unit volume of pure liquid, R is the radius of the single bubble, and $\dot{R}$ is the bubble radius growth rate. To complete the derivation of the numerical method, a relation to model the bubble growth is needed. Under the assumptions that bubble–bubble interactions and bubble coalescence can be neglected and that the bubbles remain spherical, the Rayleigh's formulation is adopted to model the bubble growth and collapse processes, and it is reported in Eq. (22).

$$\dot{R} = sgn(p_V - p)\sqrt{\frac{2}{3}\frac{|p_V - p|}{\rho_l}} \tag{22}$$

Three turbulence models, namely Realizable k-ε [28], k-ω Shear Stress Transport (SST) [29] and Reynolds Stress Transport Elliptic Blending (RST-EB) [30] are used and compared in this study. The first two are "eddy viscosity" models whose aim is to determine the turbulent viscosity μ_t by solving two additional transport equations, one for the turbulent kinetic energy k and one for the turbulent dissipation rate ε or the specific dissipation rate ω. They are purposely selected as the Realizable k-ε is proven to be valid in case of rotating homogeneous shear flows, flat plate boundary layers with and without a pressure gradient turbulent and backward facing step separated flows, while the k-ω Shear SST is widely adopted in turbomachinery, as highlighted by the literature review proposed in the introduction. As for the RST-EB model, it solves each component of the symmetric Reynolds stresses tensor, thus it is potentially more accurate to capture complex turbulent structures.

The transport equations for the Realizable k-ε turbulence model are Eqs. (23) and (24).

$$\frac{\partial(\rho k)}{\partial t} + \frac{\partial(\rho u_i k)}{\partial x_i} = \frac{\partial}{\partial x_j}\left[\left(\mu + \frac{\mu_t}{\sigma_k}\right)\frac{\partial k}{\partial x_j}\right] + P_k - \rho\varepsilon + S_k \tag{23}$$

$$\frac{\partial(\rho \varepsilon)}{\partial t} + \frac{\partial(\rho u_i \varepsilon)}{\partial x_i} = \frac{\partial}{\partial x_j}\left[\left(\mu + \frac{\mu_t}{\sigma_k}\right)\frac{\partial \varepsilon}{\partial x_j}\right] + C_{\varepsilon 1} P_\varepsilon \frac{\varepsilon}{k} - C_{\varepsilon 2}\rho\frac{\varepsilon^2}{k + \sqrt{\nu\varepsilon}} + S_\varepsilon \tag{24}$$

P_k and P_ε are production terms, S_k and S_ε are user-specified source terms, σ_k, σ_ε, $C_{\varepsilon 1}$, and $C_{\varepsilon 2}$ are model coefficients, and ν is the kinematic viscosity of the fluid.

As for the k-ω SST turbulence model, the transport equation for k is Eq. (25), while the one for ω corresponds to Eq. (26).

$$\frac{\partial(\rho k)}{\partial t} + \frac{\partial(\rho u_i k)}{\partial x_i} = \frac{\partial}{\partial x_j}\left[\left(\mu + \sigma_k \mu_t\right)\frac{\partial k}{\partial x_j}\right] + P_k - \beta^* \rho\omega k + S_k \tag{25}$$

$$\frac{\partial(\rho\omega)}{\partial t} + \frac{\partial(\rho u_i \omega)}{\partial x_i} = \frac{\partial}{\partial x_j}\left[\left(\mu + \sigma_\omega \mu_t\right)\frac{\partial \omega}{\partial x_j}\right] + P_\omega - \beta\rho\omega^2 + (1 - F_1)\frac{2\rho\sigma_\omega^2}{\omega}\frac{\partial k}{\partial x_j}\frac{\partial \omega}{\partial x_j} + S_\omega \tag{26}$$

P_k and P_ω are production terms, S_k and S_ω are user-specified source terms, σ_k, σ_ω, β^*, and β are model coefficients.

Interestingly, ε and ω are strictly related, so the real difference between k-ε and k-ω models lies in the modelling strategy of some terms inside the equations and in the adopted coefficients. Moreover, the k-ω SST model can be considered an "hybrid" model because it behaves like a k-ε model far from the walls, and like a k-ω near them thanks to the blending function F_1, addressing the problem of the high sensitivity of k-ω models to the free flow conditions.

The Reynolds Stress Transport (RST) turbulence model in its Elliptic Blending version [31] can consider effect of turbulence anisotropy, curvature of the streamlines and swirl motion. RST models compute directly the components of the Reynolds stress tensor by solving, for each component, Eq. (27).

$$\frac{D(\overline{u_i u_j})}{Dt} = P_{ij} + \phi_{ij}^* - \varepsilon_{ij} + D_{ij}^t + \frac{\partial}{\partial x_k}\left(\nu\frac{\partial(\overline{u_i u_j})}{\partial x_k}\right) \tag{27}$$

$\overline{u_i u_j}$ is the generic Reynolds stress tensor component, P_{ij} is the turbulent production, ϕ_{ij}^* is the pressure-strain, ε_{ij} is the dissipation-rate, and D_{ij}^t is the turbulent diffusion. As opposed to the two equations "eddy viscosity" models, seven equations have to be solved for a RST model: six equations for the Reynolds stresses (i.e. one for each of the six components of the Reynolds stress symmetric tensor) and one for the isotropic turbulent dissipation-rate ε. As a consequence, RST models are more computationally expensive than "eddy viscosity" ones.

The main difference between the RST model versions lies in the definition of the pressure strain ϕ_{ij}^*. The RST-EB model is based on a blending of near-wall and weakly inhomogeneous models for the pressure-strain and dissipation, as shown in Eq. (28).

$$\phi_{ij}^* - \varepsilon_{ij} = \left(1 - \alpha^3\right)\left(\phi_{ij}^w - \varepsilon_{ij}^w\right) + \alpha^3\left(\phi_{ij}^h - \varepsilon_{ij}^h\right) \tag{28}$$

w refers to the near-wall formulation, h to the weakly inhomogeneous formulation, and α to the lending parameter, which is the solution of the elliptic equation represented by Eq. (29).

$$\alpha - L^2\nabla^2\alpha = 1 \tag{29}$$

The length-scale L is defined as in Eq. (30).

$$L = C_l max\left(\frac{k^{3/2}}{\varepsilon}, C_\eta\frac{\nu^{3/4}}{\varepsilon^{1/4}}\right) \tag{30}$$

As for the near-wall flow modelling, the "two-layer all-y^+" approach is adopted for all the turbulence models. Thanks to this hybrid approach, a proper calculation of the wall quantities is ensured regardless the y^+ value.

The impeller rotation and its interaction with the surroundings can be modelled with three different approaches [32], which are compared in this study and briefly resumed in the following.

- In a "frozen rotor" simulation, a rotating reference frame is applied to the mesh region containing the impeller blades. The remaining mesh is either static or has a different rotating reference frame (as multiple

regions can have different reference frames). Centrifugal and Coriolis forces are added to the momentum equation through additional source terms to consider rotation, but both simulation and mesh are steady. As the impeller blades are frozen in space with respect to the rest of the pump, the flow field depends on their relative position. Different relative positions can result in different solutions, which is the main drawback of this approach.

- In a "mixing plane" analysis, the problem of relative positioning is overcome by using a mixing plane interface to couple the rotor and stator regions. Flow conditions on either side of the mixing plane interface are averaged circumferentially to provide a single radial/axial profile that is applied to all the cell faces at the interface.
- The "sliding mesh" approach is a rotating motion interface. In this case the mesh actually rotates. Therefore, a transient simulation is needed. Compared to the others, the sliding mesh approach has less approximations, but it is more computationally expensive.

For each pump, the fluid domain is divided into three parts (intake pipe with pump admission, rotating region, and volute with exhaust pipe). The first part extends from the inlet of the intake pipe to the impeller inlet, while the third one extends from impeller outlet to the exit of the exhaust pipe. In addition, extrusions are considered at the inlet and outlet of the intake and exhaust pipes, respectively. Each extrusion has a length equivalent to five hydraulic diameters, to develop the flow and improve the numerical stability. The second part, namely the rotating region, is the one enveloping the impeller and affected by the rotational approach (frozen rotor, mixing plane, or sliding mesh). Therefore, the outer boundaries of the region have to exhibit axial symmetry. The downstream interface of the rotating region is a cylindrical surface located midway between the impeller tip and the volute tongue, with radius equal to the arithmetic mean of the impeller and minimum volute radii. This choice provides a reasonable separation between the rotating and stationary domains, ensuring numerical stability and minimizing the influence of the interface on the main flow structures. The upstream interface of the rotating domain is placed ahead of the impeller leading edges, at a distance sufficient to ensure that the inflow to the rotating region is fully developed and unaffected by rotational effects.

Concerning the boundary conditions, pump inlets are associated with a total pressure, a turbulent intensity of 5 %, and a turbulent length scale equivalent to 3.8 % of the inlet diameter. Instead, the outlet is associated with a mass flow rate. Each other boundary is set as wall. Static walls inside the rotating region and rotating walls inside the static regions are managed by imposing tangential velocities to them.

For transient simulations, the time-step is constant and equivalent to a 1° rotation of the impeller. Each time-step is solved by twenty inner iterations of an implicit differentiation scheme. The quantities presented in this study for transient simulations are average values on a sufficient number of time-steps (i.e. usually three impeller rotations), measured after a stable behaviour is reached.

Each region of the fluid is meshed separately to avoid any influence of the relative position between impeller and volute on the mesh. In this way, it is possible to correctly apply the rotational approaches aforementioned. The mesh is made of polyhedral cells with prismatic layers on each solid wall. Finer cells are used for the impeller and the volute, where it is harder to simulate the flow behaviour. In addition to that, inlet and outlet extrusions are meshed by extruding the polyhedral mesh to reduce the total number of cells and minimize numerical diffusion.

A mesh sensitivity analysis is conducted for both the pumps, using a single-phase sliding mesh approach and the k-ω SST turbulence model, to find grids able to ensure grid-independency of the results. For this analysis, both the investigated pumps are simulated at the highest rotational velocity and flow rate available from the experimental data, to test the grid capabilities at the most stressing conditions. The mesh sensitivity analysis is carried out with the sliding mesh approach, but it remains valid also for the other ones.

The selected mesh for pump X has 782,357 cells, with only three prismatic layers. The first prismatic layer is 0.1 mm thick, leading to y^+ values in between 30 and 100 in the entire domain, thus the hybrid wall treatment behaves as a high-Reynolds one. The stretch factor among the layers is 1.5. The minimum surface size is 1.0 mm, which is reduced to 0.5 mm on impeller and volute, while the target surface size is 5.0 mm. The average diameter (i.e. the diameter of a sphere with the same volume as the average cell volume) of bulk cells is 1.02 mm in the impeller region, 1.16 mm in volute and discharge duct, and 3.10 mm in the suction duct. As visible in Fig. 7(a), the selected mesh gives results with a deviation of less than 1 % compared to a significantly finer grid with 20 million cells. Interestingly, the latter employs much smaller bulk cells and fifteen prismatic layers, leading to an average y^+ around 1 in the entire domain. Therefore, with this grid, the hybrid wall treatment behaves as a low-Reynolds one.

Concerning pump Y, it requires a finer mesh with 2.6 million cells, characterized by ten prismatic layers, which lead to a behaviour of the near-wall treatment comparable to a low-Reynolds one. Indeed, the first prismatic layer is 0.005 mm thick, then the stretch factor among the layers is 1.5. Minimum and target surface sizes are 0.5 mm and 5.0 mm, respectively, which are the same values used for pump X. The average diameter of bulk cells is 0.95 mm in the impeller region, 1.50 mm in the volute and discharge duct, and 1.98 mm in the suction duct. Therefore, the mesh is heavier because of both increased number of prismatic layers and dimensions (in fact pump Y is slightly bigger than pump X). The mesh sensitivity results for pump Y are reported in Fig. 7(b). Also in this case, the deviation with respect to the reference (finest) mesh is less than 1 %.

3.2. Results

3.2.1. Non-cavitating conditions – Turbulence model sensitivity

The first part of this section deals with non-cavitating conditions. Initially, the results on turbulence model sensitivity are presented. Based on the available literature, the Realizable k-ε and the k-ω SST are some of the most widely employed turbulence models for centrifugal pumps. Instead, more advanced models, like the RST-EB one, are almost completely neglected due to their complexity and computational cost. The sensitivity proposed in the following aims at comparing the models mentioned above, by using a sliding mesh approach and a single-phase physics, in order to assess the predictive capabilities of both consolidated and advanced models. A single rotational velocity is selected for all the simulations of a given pump, which is, for both the machines, the highest velocity of the respective experimental datasets. The velocity values are purposely selected as representative of significant engine conditions. Moreover, a high rotational velocity ensures that any effect of the Reynolds number on the performance is filtered out. Mass flow rate and total pressure are imposed at inlet and outlet, respectively, and both are changed accordingly to the experimental data for each simulation. The single-phase physics makes the imposition of an inlet pressure a purely numerical requirement, because it is used only as a reference value for the pressure field. In other words, it does not affect the head calculation at non-cavitating conditions. To ensure a proper comparison between CFD and experiments, the numerical pressures are measured on the same sections where the sensors are placed in the test bench. Similarly to the experiments, the numerical results are presented in terms of FC and HC.

As it is visible in Fig. 8, the "eddy viscosity" turbulence models provide very similar results, even if the Realizable k-ε tends to slightly lose accuracy compared to the k-ω SST for very low and very high FCs. At the same time, the k-ω SST turbulence model predicts the flow behaviour adequately even in extreme off-design conditions.

The RST-EB is generally more accurate than the "eddy viscosity" models, as it is visible for pump X in Fig. 8(a). This is confirmed in quantitative terms by Table 4, reporting accuracy and computational time. In this regard, it is useful to point out that, due to lower numerical

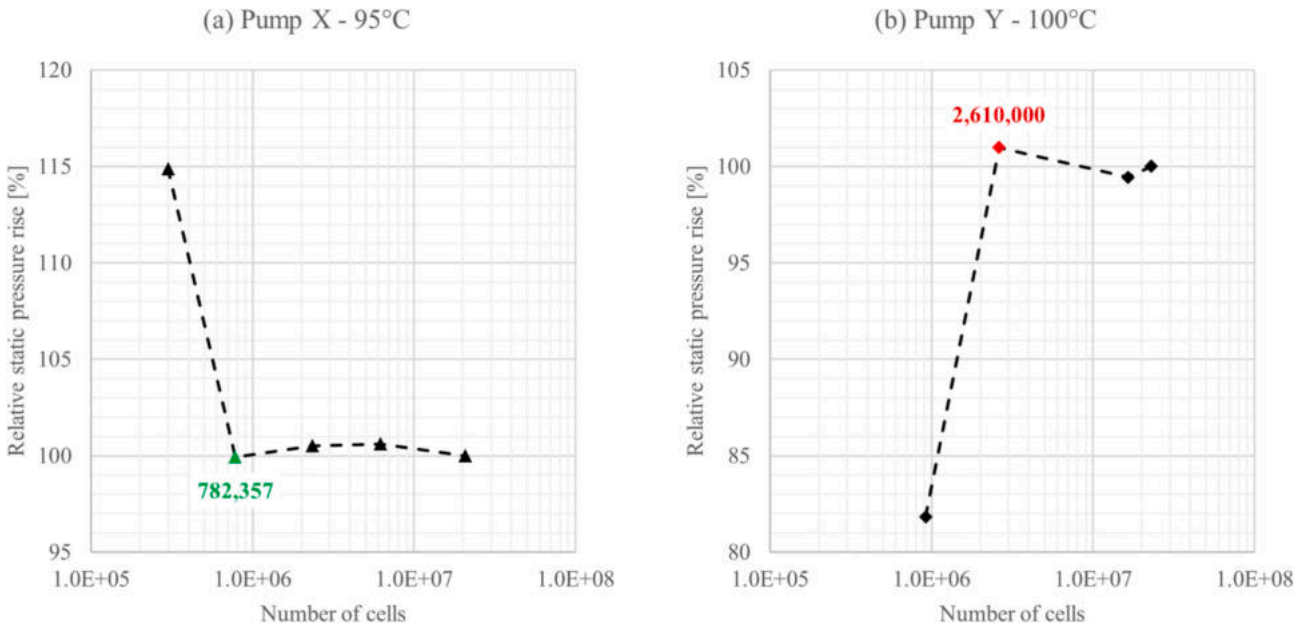

Fig. 7. Mesh independency study for (a) pump X and (b) pump Y. Both pumps are simulated at their respective maximum rotational velocity and flow rate available from experimental data.

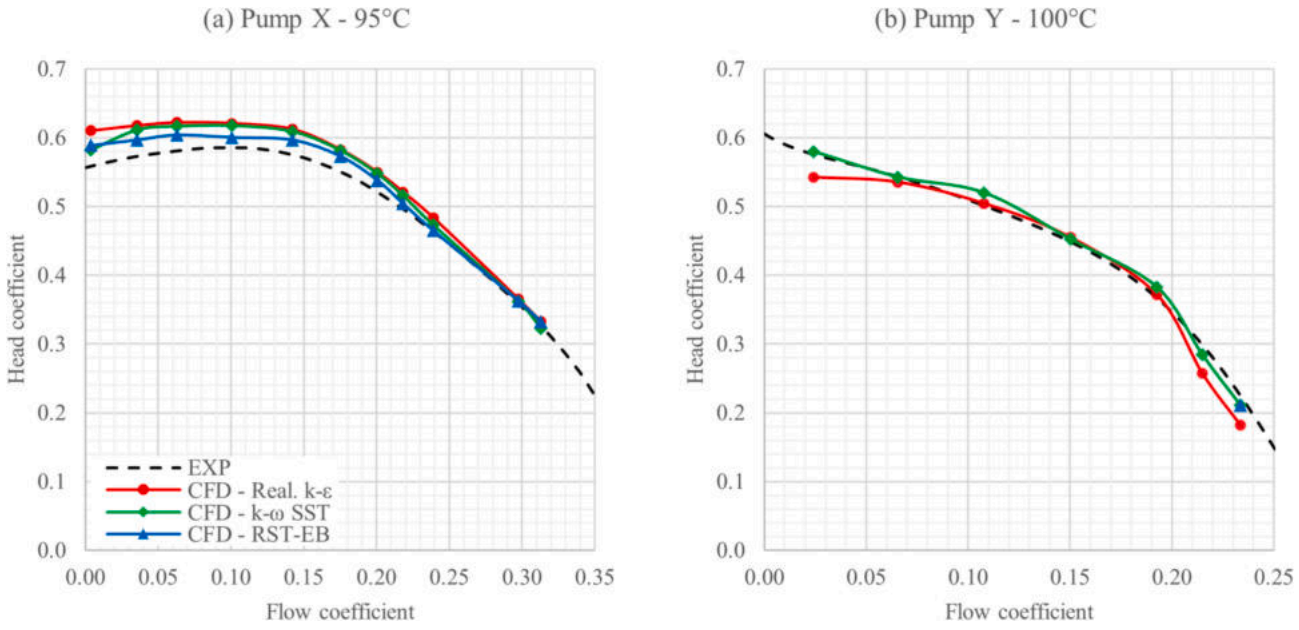

Fig. 8. Comparison between Realizable k-ε, k-ω SST and RST-EB turbulence models, using a sliding mesh single-phase setup, for (a) pump X and (b) pump Y.

stability, the RST- EB requires a computational time that is twice those of k-ε and k-ω. This problem gets more critical considering pump Y, due to the complex geometry. Indeed, the RST model requires a lower time-step, corresponding to 0.1° of rotation (instead of 1° used for all the other simulations). Considering the huge increase in the computational time, only the maximum FC condition is simulated. As it is visible in Fig. 8(b) for pump Y, the RST model does not improve the already satisfactory performance of the SST k-ω. They provide almost identical results in the last operating condition, and both are very close to the experiment.

Considering the slightly lower accuracy of the Realizable k-ε at some conditions and the extremely high computational cost of the RST-EB model, whose accuracy is not sensibly higher than k-ω SST, the latter is found to be the best choice for this application. In this regard, it is interesting to notice that only one FC is tested with the RST-EB for pump Y. The reason is the extremely high computational cost, which increases by one order of magnitude. Considering that the eddy viscosity models are able to provide accurate results with much lower effort, the validation of the RST-EB at further conditions seems to be useless.

3.2.2. *Non-cavitating conditions – Rotational approach sensitivity*

Once a suitable turbulence model is selected, it is necessary to clarify the capabilities of the three rotational approaches previously introduced, namely frozen rotor, mixing plane, and sliding mesh. Their results are compared against the experimental data on both pumps, to determine accuracy and computational cost. This analysis is performed using a single-phase physics, the k-ω SST (identified as the best turbulence model in the previous sensitivity) and, for a given pump, the same

Table 4
Accuracy and computational cost of the different turbulence models for a single-phase sliding mesh setup. All the simulations are solved using 16 processor units in parallel.

	Pump X			Pump Y		
Turbulence model	Real. k-ε	k-ω SST	RST-EB	Real. k-ε	k-ω SST	RST-EB
Average deviation	5.5 %	4.3 %	2.9 %	6.3 %	3.0 %	5.9 %*
Standard deviation	5.9 %	4.7 %	3.3 %	9.3 %	3.7 %	5.9 %*
Maximum deviation	+9.2 %	+6.8 %	+5.4 %	−19.3 %	−6.4 %	−5.9 % *
Time to rotate 1°	15.8 s	16.1 s	27.4 s	58.3 s	58.7 s	995.3 s**

* Statistics refer to only one operating condition.
** The adopted time-step corresponds to 0.1° of rotation.

mesh across all cases. The investigated conditions are the same as the previous analysis.

As visible in Fig. 9(a), the three approaches applied to pump X behave in a similar way around the best efficiency FC equal to 0.18, while mixing plane and frozen rotor lose their accuracy when off-design FCs are considered. Instead, the sliding mesh approach maintains a good agreement with the experimental data across the entire range of conditions, especially for high FCs. The mixing-plane approach tends to underestimate the HC, at low FCs, by less than 5 %. However, at high FCs, it overestimates the HC by almost 30 %. On the contrary, the frozen rotor approach underestimates performance at high FCs by more than a 10 % and it overestimate the HC at low flow coefficients by almost 20 %. When the sliding mesh approach is employed, the deviation from experiments remains in a range between −1.3 % and 6.8 %, making it a more accurate methodology compared to mixing plane and frozen rotor.

Moving to pump Y, Fig. 9(b) shows the results of mixing plane, frozen rotor and sliding mesh. The frozen rotor method shows a similar trend to those observed for pump X, overestimating HC (+15 %) at low FCs, and underestimating HC at high FCs (–32 %). The mixing plane is accurate when the FC is beyond 0.10, but underestimates HC (−14 %) at low FCs. Lastly, the sliding mesh method is again the most accurate, keeping the maximum deviation from experimental data below 6.4 % and the average deviation at 3.0 %.

If both pumps are considered, the sliding mesh method outperforms both mixing plane and frozen rotor for what concerns accuracy. Table 5 gives more insight into this comparison, by also considering the calculation times associated with each method. Even though the time required by each iteration is similar for the three methods, because they are compared with the same mesh, the unsteady nature of the sliding mesh approach demands for much more iterations to provide reliable results. Indeed, each time-step requires twenty iterations, and 360 time-steps are needed for one complete rotation of the impeller. On top of that, the simulation has to reach a periodic stability, which is usually obtained after several rotations of the impeller, and, only after that, a result can be obtained by averaging the quantities over three impeller revolutions. This means that, compared to steady-state methods that usually require roughly 5000 iterations to meet convergence, the sliding mesh approach needs approximately 72,000 iterative steps. This explains why the sliding mesh approach requires about fifteen times the computational cost of a steady-state method. On the other hand, the sliding mesh method is the only one able to provide accurate results when tested on pumps characterized by complex geometrical features.

In order to better appreciate the differences between the different rotational approaches, the resulting pressure field is analyzed in the

Table 5
Accuracy and computational cost between the three rotational approaches for both pumps. All simulations are solved using 16 processor units in parallel.

	Pump X			Pump Y		
Approach	Mixing plane	Frozen rotor	Sliding mesh	Mixing plane	Frozen rotor	Sliding mesh
Average deviation	6.8 %	6.5 %	4.3 %	7.5 %	12.2 %	3.0 %
Standard deviation	10.4 %	10.3 %	4.7 %	8.6 %	14.1 %	3.7 %
Maximum deviation	+26.7 %	+19.4 %	+6.8 %	−13.7 %	–32.4 %	−6.4 %
Iterations	5 000	5 000	72 000*	5 000	5 000	72 000*
Time per iteration	1.20 s	1.15 s	1.00 s	3.20 s	3.10 s	2.95 s
Total time	1.67 h	1.60 h	20.00 h	4.44 h	4.31 h	59.00 h

* Corresponding to 3,600 time steps.

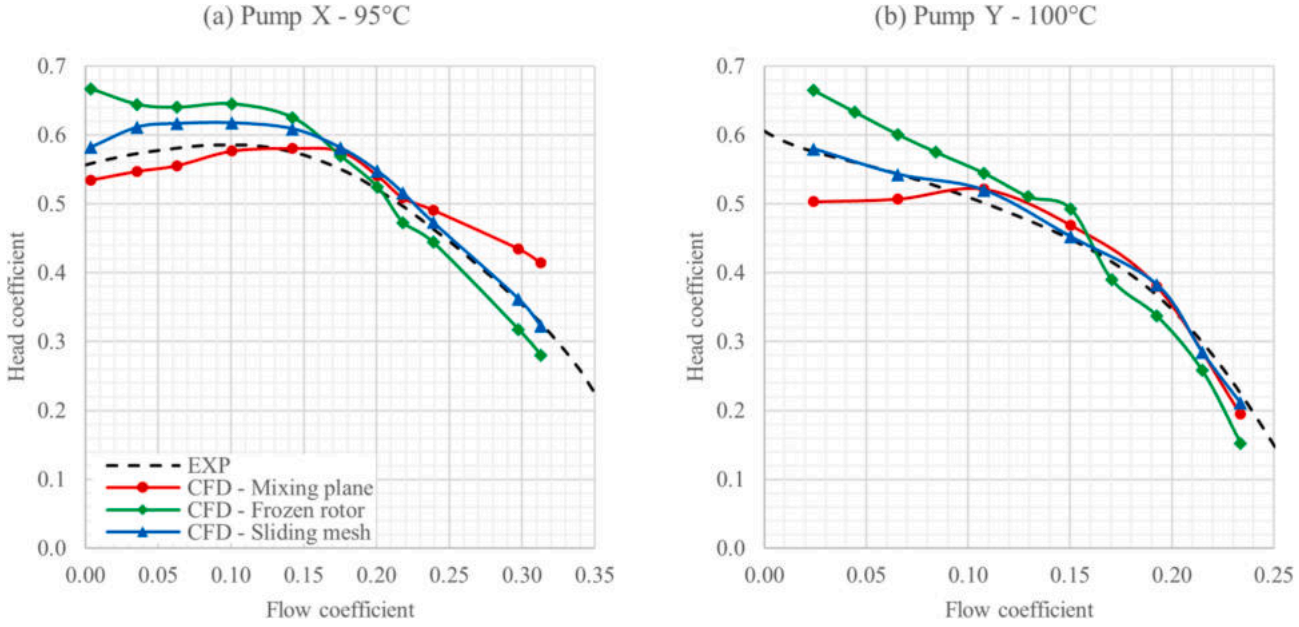

Fig. 9. Comparison between mixing plane, frozen rotor and sliding mesh approaches using single-phase physics and the k-ω SST turbulence model against experimental data for (a) pump X and (b) pump Y.

following. Considering a steady-state methodology, what happens inside the rotor region is calculated with the Moving Reference Frame (MRF) approach, which consists in rewriting the transport equations in a rotating reference frame and, thus, including apparent forces in the calculation.

On top of that, the mixing plane interface employs a circumferential averaging technique which is meant to replicate the mean behaviour of the pump. The flow quantities are averaged through the interface, resulting in a very symmetrical pressure field which is not influenced by the relative position between the impeller and the volute. It must be noted that the mixing plane approach generates non-continuous flow fields through the interface because the quantities are spatially averaged before crossing it, as it can be seen in Fig. 10(1.a)(2.a) and Fig. 11(1.a)(2.a). In that way, information about complex flow structures, such as vortices and wakes, are lost through the interface, lowering the accuracy of the simulations.

Instead, a frozen rotor approach makes the interface between rotor and stator communicate information directly from one side to the other. Therefore, the interaction between the impeller and the volute is taken into account, which gives highly asymmetrical pressure fields as it can be seen in Fig. 10(1.b), (2.b) and Fig. 11(1.b), (2.b). In particular, considering pump X, the low pressure zone is closer to the volute tongue for overflow conditions (Fig. 10(2.b)), and more distant for underflow conditions (Fig. 10(1.b)). This behaviour is probably influenced by the relative position between impeller and volute, whose effect can be considered only by simulating different impeller positions.

Finally, the sliding mesh approach is the simplest and most accurate one because the grid of the rotor region actually rotates during the simulation, reducing approximations only to the interpolation of the quantities through the interface, but requiring unsteady simulations, which are more computationally demanding than the steady ones. This method not only considers the relative position between impeller and volute, but also the dynamic effects inside the pump. Indeed, the outlet pressure signal regularly fluctuates with a frequency equal to the blade passing frequency (i.e. the inverse of the time required by the impeller to cover the blade-to-blade angle). Instead of the space-average performed by the mixing plane approach, in a sliding mesh simulation the performance parameters of the pump can be obtained by time-averaging the flow quantities over a sufficiently large period of time. The instantaneous flow fields are still asymmetrical, but less than in the frozen rotor approach, as it is shown by Fig. 10(1.c), (2.c) and Fig. 11(1.c), (2.c).

The mixing plane and the frozen rotor methods are reliable to study the design operative conditions of a centrifugal pump, but they lose their accuracy when more complex structures appear in the flow in off-design conditions. The complexity of the flow structures is also correlated with the complexity of the pump geometry, which is higher for automotive applications due to the compactness and positioning requirements and for the vast range of operating conditions that the engine cooling systems have to face.

3.2.3. *Non-cavitating conditions – Rotational velocity sensitivity*

For a given pump, all the simulations presented until now share the same rotational speed. Indeed, the fundamental assumption behind the analyses proposed in this work is the validity of the turbomachinery affinity laws, that was proved to be, in the previous paragraphs, a reliable assumption for the experimental data. However, in order to strengthen the validation of the numerical setup, it is interesting to evaluate the methodology behaviour for different velocities. In other words, proving the validity of the assumption also for CFD simulations is important to exclude the rotational velocity as a parameter on which to

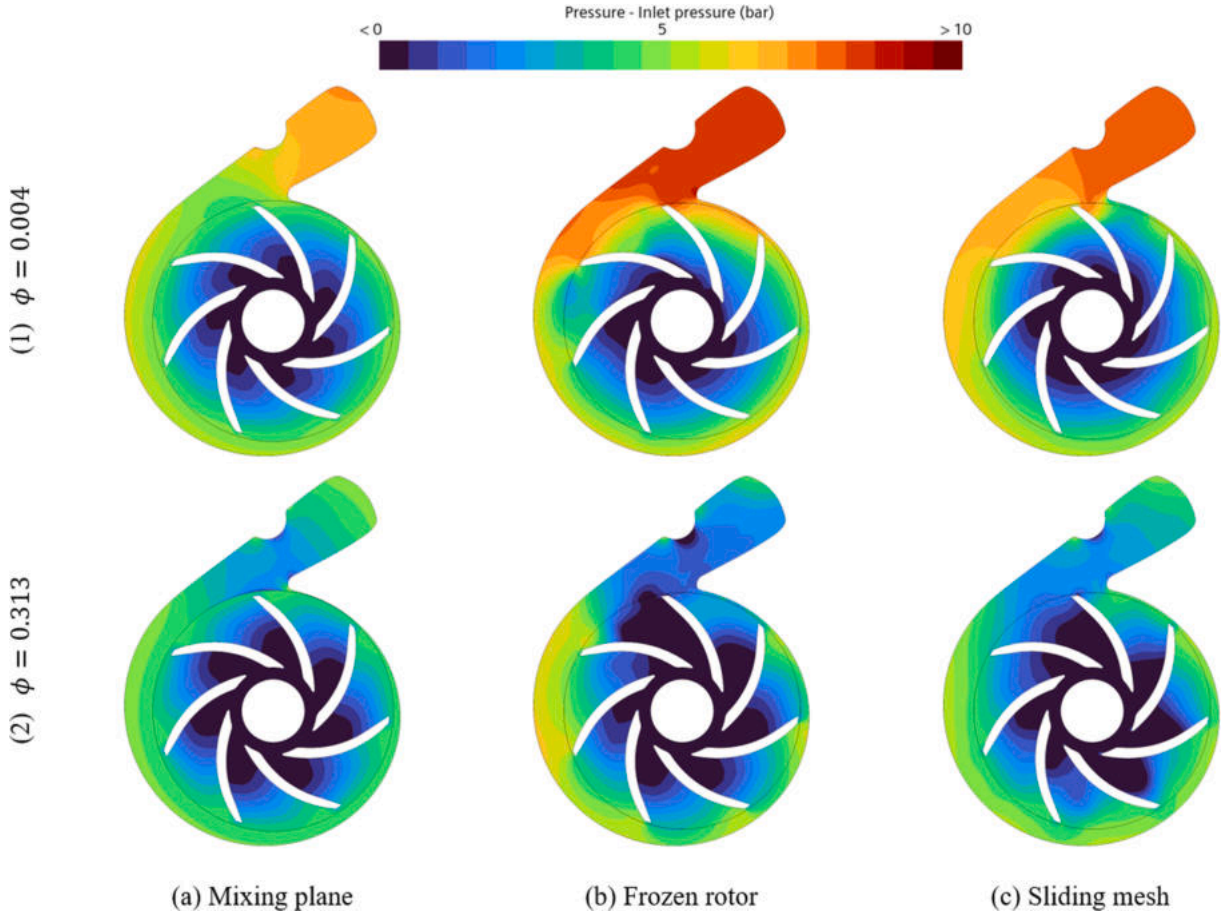

Fig. 10. Pressure difference ($p - p_{S,1}$) in a section of pump X (95 °C). The three rotational approaches are compared at two different flow coefficients.

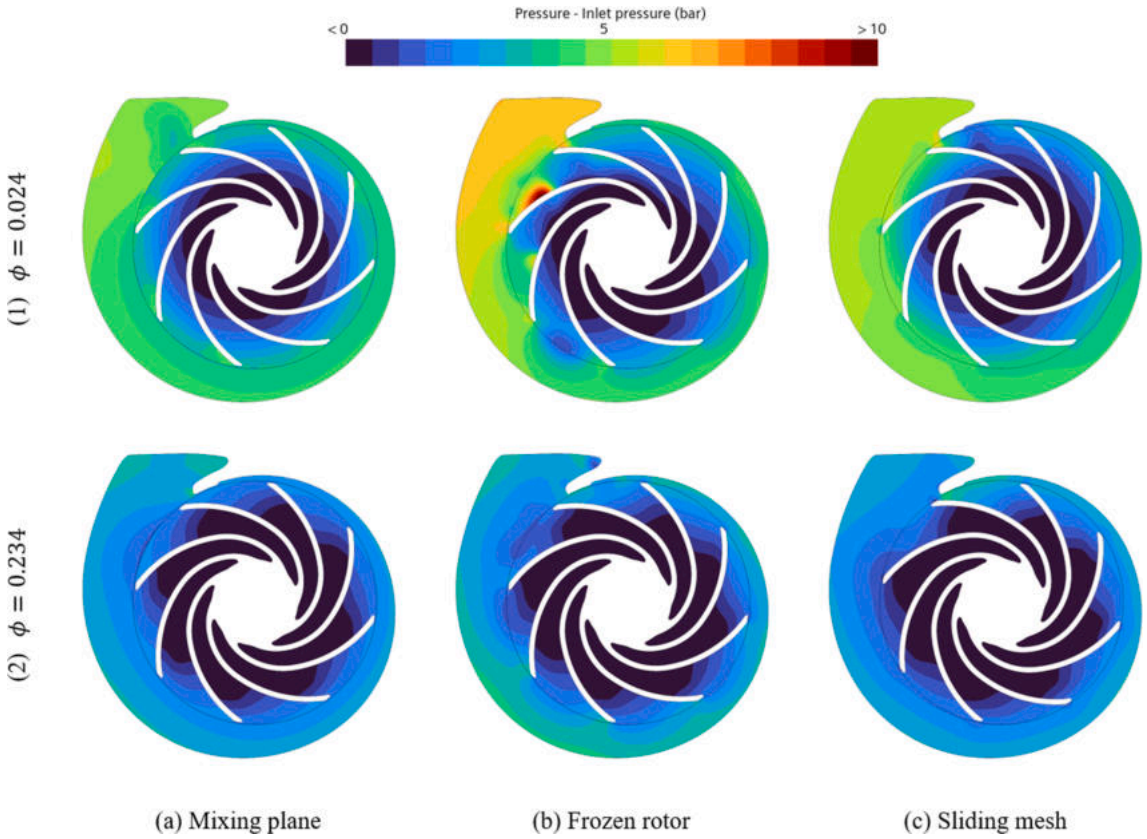

Fig. 11. Pressure difference ($p - p_{S,1}$) in a section of pump Y (100 °C). The three rotational approaches are compared at two different flow coefficients.

focus and, in this way, to reduce the number of variables to consider for the numerical analyses.

Fig. 12 presents experimental data and CFD results in terms of relative total pressure rise $\Delta p_{T,r}$ against relative flow rate Q_r for different rotational velocities. The CFD setup is inherited from the previous sensitivity analyses. Overall, all the experimental curves are well predicted by the single-phase sliding mesh methodology, with standard deviations below 6.0 % for each considered velocity, as reported in Table 6.

A more detailed analysis is presented in Fig. 13, where the previous head curves are presented in terms of dimensionless parameters (HC and FC). CFD and experiments show a satisfying agreement for pump X, in

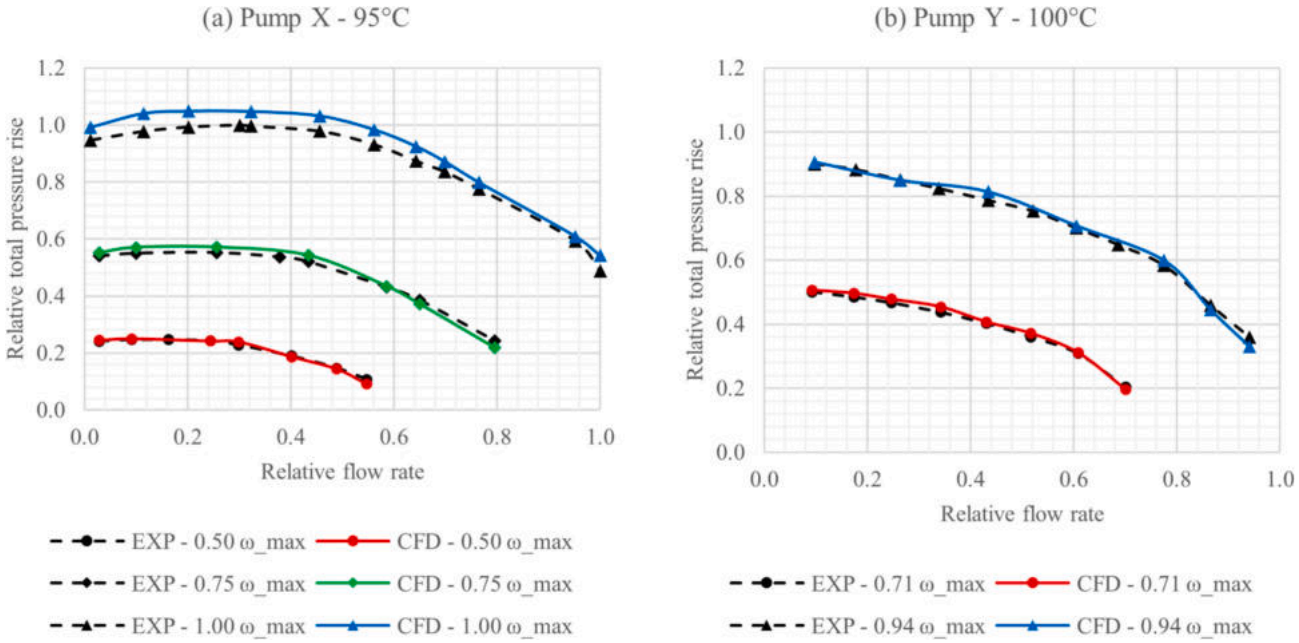

Fig. 12. Comparison between CFD and experimental data using sliding mesh approach, single-phase physics and k-ω SST turbulence model. Curves corresponding to different rotational velocities are compared using relative quantities.

Table 6
Accuracy for the single-phase sliding mesh methodology, at different rotational velocities.

	Pump X			Pump Y	
Rotational velocity	$0.50 \cdot \omega_{max,X}$	$0.75 \cdot \omega_{max,X}$	$1.00 \cdot \omega_{max,X}$	$0.71 \cdot \omega_{max,Y}$	$0.94 \cdot \omega_{max,Y}$
Average deviation	1.5 %	1.9 %	4.3 %	3.7 %	3.0 %
Standard deviation	1.9 %	2.5 %	4.7 %	6.0 %	3.7 %
Maximum deviation	4.2 %	4.2 %	6.8 %	−5.3 %	−6.4 %

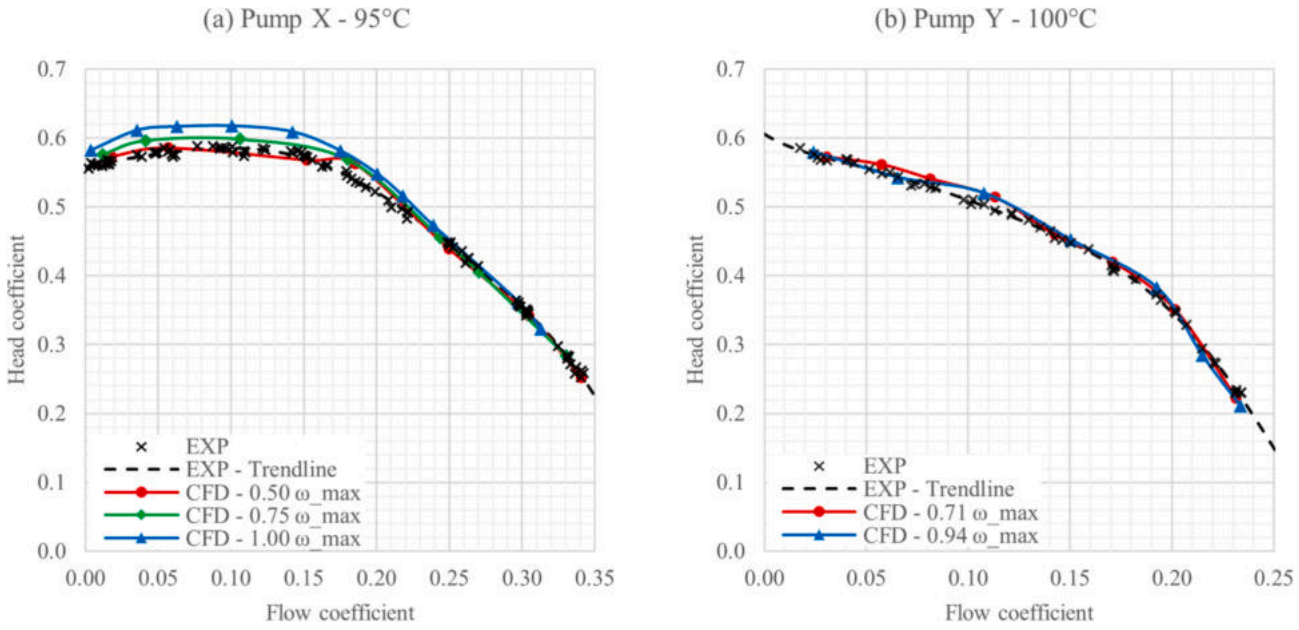

Fig. 13. Comparison between CFD and experimental data using sliding mesh approach, single-phase physics and k-ω SST turbulence model. Curves corresponding to different rotational velocities are compared using dimensionless coefficients.

particular at high FCs, and an excellent agreement for pump Y. As for pump X at low-to-medium FCs, a slight deviation is noticed especially increasing the speed. Overall, the CFD framework is able to correctly predict the effect of speed on the pump performance.

3.2.4. Cavitating conditions – Turbulence model sensitivity

The combination of sliding mesh approach, single-phase physics, and k-ω SST turbulence model is a sufficiently accurate framework for the prediction of pump performance in non-cavitating conditions. Nevertheless, this is not enough to fully characterize the fluid dynamic behaviour of a pump. Indeed, it is well known that one of the main problems which affect pumps is cavitation. Considering all the disadvantages related to that phenomenon (such as noise, vibration, flow instabilities, performance degradation, surface damage and, in the worst cases, system failure), it is of paramount importance to be able to predict it in order to improve the pump design. CFD is a powerful tool even in this case, but a more advanced approach than the one used for non-cavitating conditions must be adopted. In fact, the single-phase physics can give just a limited amount of information regarding cavitation, because it cannot consider bubble formation and collapse. Therefore, a multi-phase simulation physics is needed. In this study, it relies on the Volume of Fluid (VOF) method coupled with the Schnerr-Sauer cavitation model. Sensitivity analyses to rotational approach and turbulence model are again proposed in the following for cavitating conditions. In fact, it is not obvious that models that are effective under non-cavitating conditions still provide accurate results under cavitation.

In this section, the sensitivity analysis to turbulence models already carried out for non-cavitating conditions is expanded to cavitating ones thanks to a multi-phase numerical setup. The RST Elliptic Blending model is not tested because of its high computational cost and considering that, as it will be shown in the following, eddy viscosity models are able to provide reliable results with much lower effort. Therefore, only Realizable k-ε and k-ω SST are compared and tested for the prediction of the PF curves of both pumps.

In this case, the strategy starts from a simulation with a sufficiently high inlet pressure (corresponding to $\sigma = 5.0$), representing non-cavitating conditions and whose HC is used as reference value (denominator) for the PF computation. Keeping the same flow rate, rotational velocity, and fluid temperature (i.e. same FC), other simulations with gradually reduced inlet pressures (and CNs) are carried out until the HC (and the PF) of the pump drops. For high CNs, the multi-phase setup (which includes the VOF method and Schnerr-Sauer cavitation model) gives the same values of HC as those predicted by the single-phase setup. However, even if in non-cavitating conditions the VOF method does not handle vapor, the addition of transport equations makes simulations heavier (+64 % of computational time).

It is worth to point out that gradually reducing the inlet pressure is the standard experimental procedure for creating head loss curves and evaluating cavitation in pumps. In fact, since the rotational velocity has an effect on the simulated HC of the pumps in non-cavitating conditions (Fig. 13), changing the inlet pressure is considered a safer simulation methodology to address cavitation. Instead, the experimental data presented in this work are obtained mainly by changing the rotational velocity of the impeller. For this reason, CFD and experiments can be compared only by using dimensionless coefficients (FC, HC, CN, and PF).

Overall, the results in Fig. 14 provided by the two turbulence models closely resemble each other and both are able to properly predict the cavitation onset, i.e. the drop of PF when CN lowers. However, the PFs associated with each set of simulations (i.e. each coloured curve of Fig. 14) depend on the HC value obtained by the simulation with the

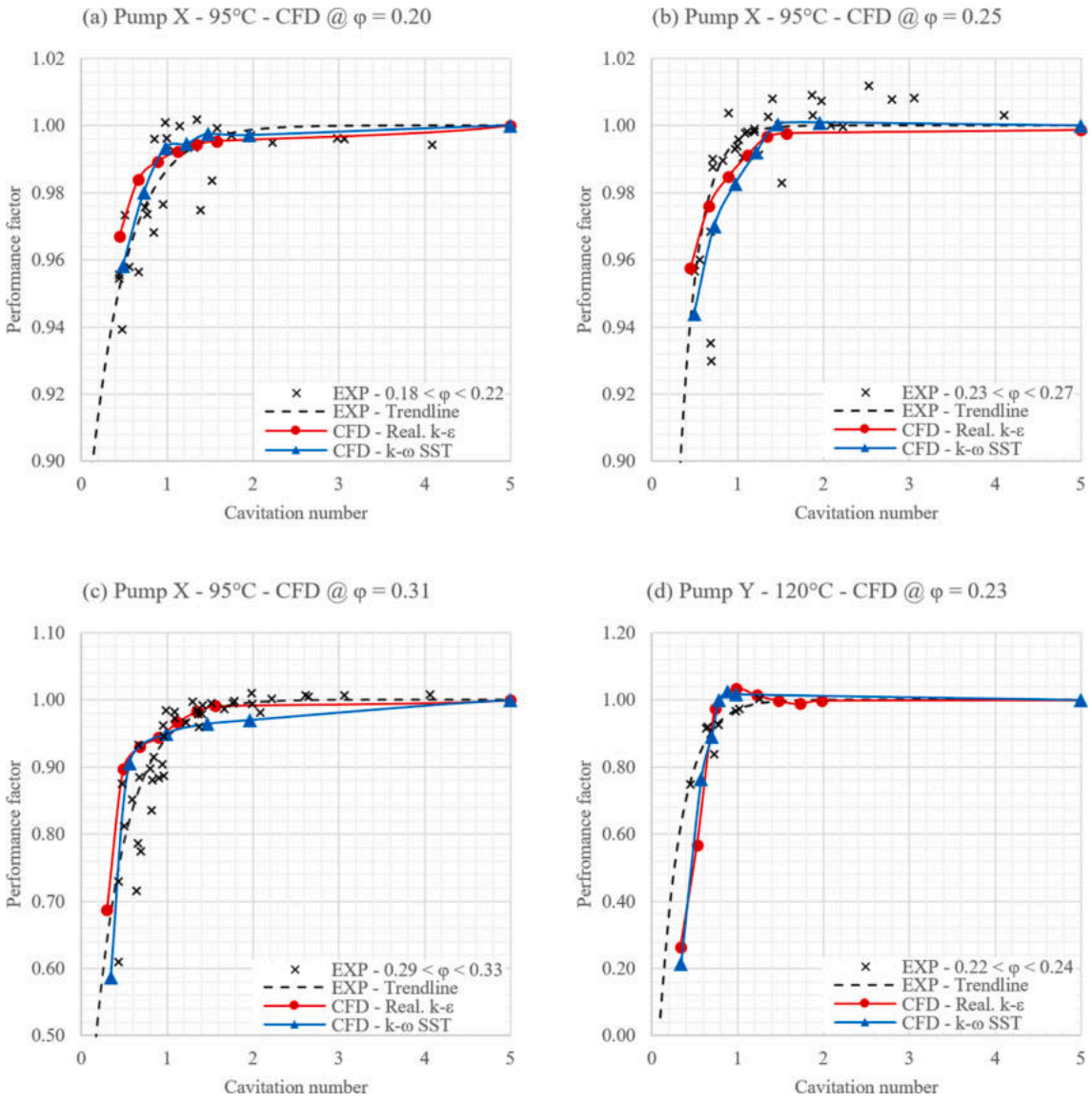

Fig. 14. Comparison, in terms of cavitating performance curve, between Realizable k-ε and k-ω SST turbulence models, using a sliding mesh multi-phase setup, for pump X at (a) $\varphi = 0.20$, (b) $\varphi = 0.25$, and (c) $\varphi = 0.31$ (c), and for pump Y at (d) $\varphi = 0.23$.

highest CN inside that particular set. To clarify this, it is possible to consider Fig. 14(c). When $\sigma = 5.0$, even if the value of PF is 1.0 for experiments and both CFD curves, the values of HC are slightly different. These differences are already addressed in the previous sections dealing with non-cavitating conditions, so the analysis in cavitating conditions only focuses on the capability of the CFD models to accurately capture the shape of the experimental PF curves. In this sense, performance and cavitation are decoupled and separately analysed. As further example, a method can be inaccurate in predicting pump performance (i.e. HCs in non-cavitating conditions) but it can be accurate in predicting cavitation (i.e. the shape of PF curves as a function of the CN).

In this case, even though both turbulence models adequately capture cavitation, the k-ω SST must be preferred to the Realizable k-ε because the former shows better predictive capabilities in non-cavitating conditions.

3.2.5. *Cavitating conditions – Rotational approach sensitivity*

In this paragraph, the three rotational approaches are again compared under cavitation. The goal of this further comparison is to confirm the better capabilities of the sliding mesh approach. In fact, since it is the most demanding one, it is important to justify, also with cavitation and a multi-phase physics, the actual need of increased computationally cost. In this regard, it is interesting to point out that, given the intrinsically time-dependent nature of cavitation, all the approaches are now tested in a transient simulation framework. This removes the main advantage of the mixing plane and frozen rotor techniques, which is the possibility to run steady-state simulations. Nevertheless, their computational cost is still lower than that of the sliding mesh approach, as the latter requires the solution to be periodically stable, which generally takes longer time than that needed to stabilise the solution around a constant value. Overall, the sliding mesh approach computational cost is still an order of magnitude higher compared to the other methodologies.

Results (Fig. 15) show that the sliding mesh approach is the most accurate one to predict the head loss curve for each of the analysed flow coefficients, and for both pumps. In general, mixing plane and frozen rotor tend to underestimate the head loss due to cavitation and, on the complex geometry of pump Y, they lose much of their predictive capability. In particular, considering pump Y in Fig. 15(d), the mixing plane approach gives values of PF around 1.35 when CN is in the range between 0.55 and 0.75, where the sliding mesh approach correctly predicts the performance drop seen in the experimental data. The mixing plane

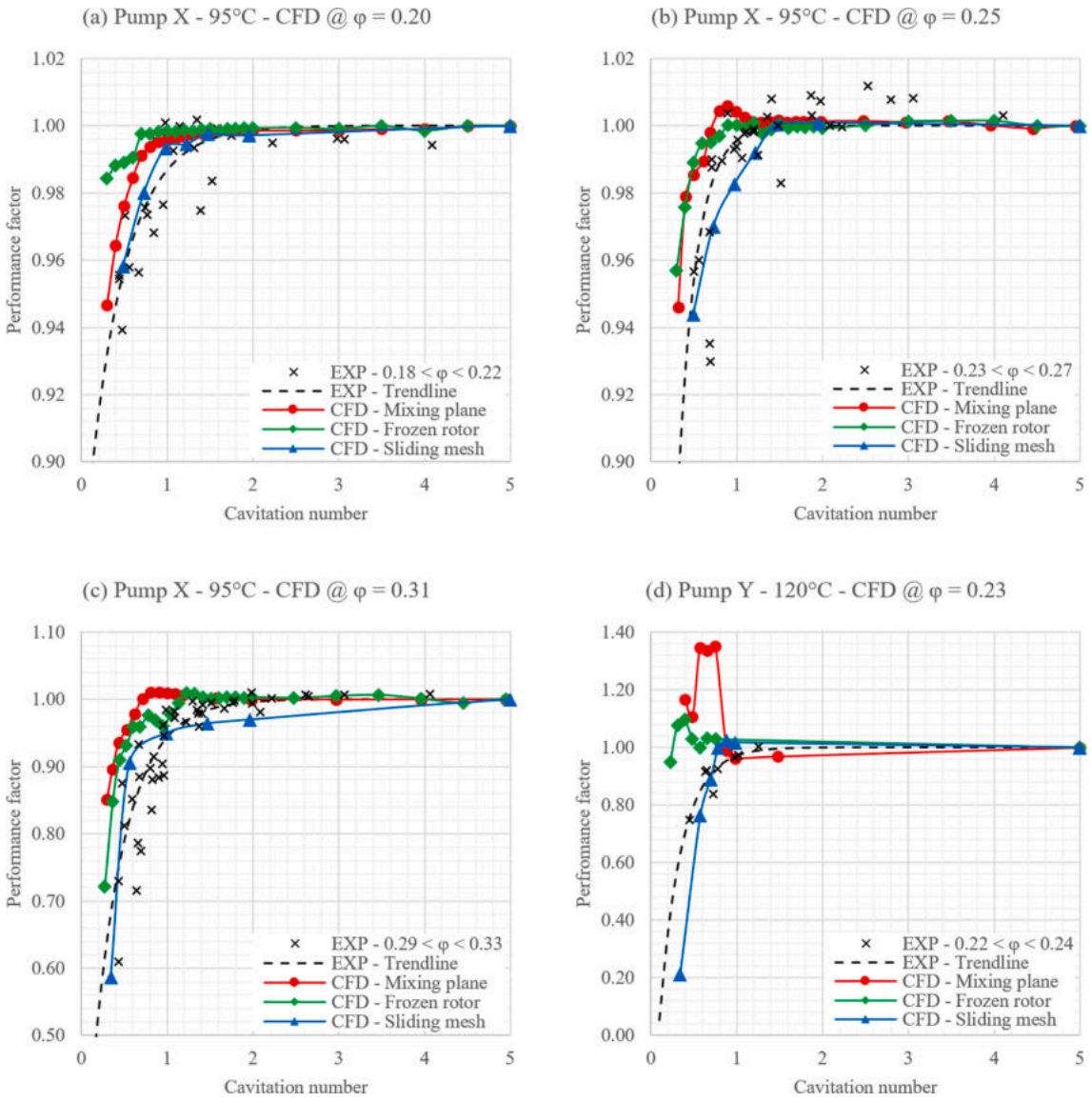

Fig. 15. Comparison, in terms of cavitating performance curve, between rotational approaches (mixing plane, frozen rotor and sliding mesh), using a multi-phase-phase setup and the k-ω SST turbulence model, for pump X at (a) $\varphi = 0.20$, (b) $\varphi = 0.25$, and (c) $\varphi = 0.31$ (c), and for pump Y at (d) $\varphi = 0.23$.

shows an increase of performance before the cavitation breakdown (i.e. the dramatic loss of performance which happens below the critical CN), which is a phenomenon that may arise in some pumps, but it is not the case of pump Y. Furthermore, a 35 % of performance increase before breakdown is an unrealistic value, proving that the mixing plane fails on complex geometries. Moving to the frozen rotor approach, it gives more reasonable results than the mixing plane, but still presents a performance overshoot before the head loss and it underestimates the cavitation. Therefore, it is possible to conclude that, similarly to non-cavitating conditions, the sliding-mesh approach is the only one able to provide reliable results with complex geometries, despite the higher computational cost.

To expand the analysis on the rotational approaches under cavitating conditions, it is useful to visualise the vapor distributions inside both the pumps, as reported in Fig. 16.

Starting from pump X and on equal conditions between all the rotational approaches, it is possible to see that cavitation mostly affects the suction side of the impeller blades, but differences can be noticed among the approaches. The mixing plane filters out the interaction between the impeller and the volute through the interface. Therefore, the vapor cavities are homogenously distributed on all the blades, as visible in Fig. 16(1.a). Instead, with the frozen rotor approach (Fig. 16(1.b)), the inter-blade channel close to the volute tongue is almost completely obstructed by cavitation, while the other blades are much less affected. Additionally, vapor is also present outside the blade external diameter, suggesting a super-cavitating behaviour, and near the convex geometrical feature of the discharge channel. Lastly, the sliding mesh approach (Fig. 16(1.c)) shows inhomogeneous cavitation like the frozen rotor, but the most critical blades are those moving where the volute cross-section is lower. Moreover, it is possible to see small, isolated cavities, which are separated from the main ones and transported through the discharge channel until they condensate. That is a dynamic effect which is visible thanks to the rotating impeller of the sliding mesh method.

Moving to pump Y, the differences between the approaches are less visible, probably because of the narrower inter-blade channel which evens out the flow. In this case, the mixing plane approach concentrates the cavitation closer to the impeller eye, especially on the opposite side of the volute tongue (Fig. 16(2.a)). That is due to the spiral inflow channel, which already creates an inhomogeneous pressure distribution before the impeller. Therefore, even though the effect of the discharge volute is filtered out by the downstream mixing interface, the cavities are still unevenly distributed on the blades. The frozen rotor method

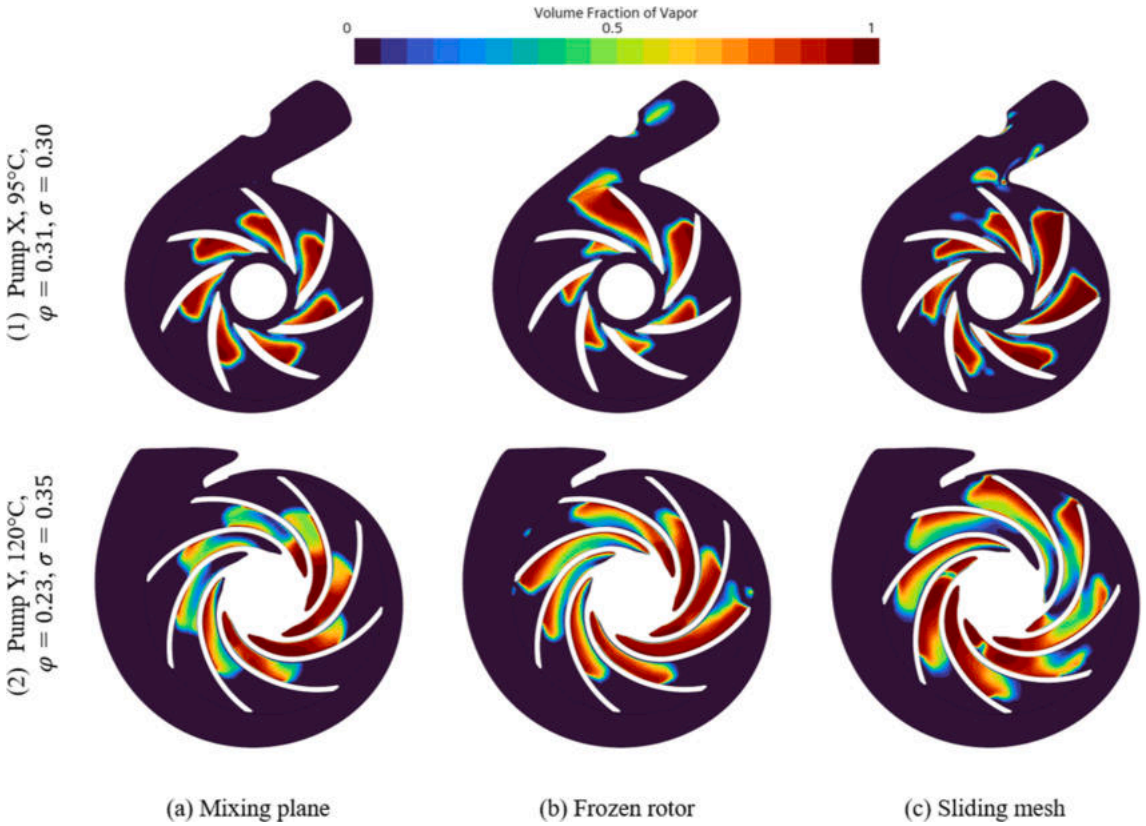

Fig. 16. Volume fraction of vapor in pump X (95 °C, $\varphi = 0.31$, $\sigma = 0.30$) and pump Y (120 °C, $\varphi = 0.23$, $\sigma = 0.35$) for the three rotational approaches using multi-phase physics.

presents a similar distribution of cavities with respect to the mixing plane but their extension is larger (Fig. 16(2.b)), which is well correlated with the lower predicted head (Fig. 15(d)). Finally, the sliding mesh approach shows the most extensive presence of cavitation, which generally covers the blades for all their length and explains the highest head loss among the predicted ones. Furthermore, the shapes of the cavities are generally less smooth than in the other methods, probably due the presence of dynamic effects that are captured thanks to the rotating impeller grid (Fig. 16(2.c)).

Considering that the sliding mesh approach is the most accurate one to predict the pump performance, it can be used to visualise the vapor cavity evolution with respect to the cavitation number, as reported in Fig. 17. In each case, cavities start to appear in a specific zone of the pump, where pressure assumes the lowest value. Then, as the cavitation number decreases, the cavities grow and appear in other regions of the pump. They gradually narrow the flow passage for the liquid, in turn increasing losses and reducing the head of the pump. When the cavities are large enough, they completely disrupt the flow, causing cavitation breakdown.

3.2.6. *Cavitating conditions – Mesh sensitivity*

Before the conclusions, it is interesting to point out that the results proposed above for pump X, under cavitation, are obtained with a different mesh compared to the one adopted for non-cavitating conditions and presented in the numerical setup section. This is related to the increased flow complexity due to cavitation, which requires a finer grid. The mesh adopted under cavitation is the result of a further sensitivity analysis. It is conducted by simulating, with a sliding mesh multi-phase approach, a pump for a combination of FC and CN associated to head loss, which is taken from the experimental data (e.g. $\varphi = 0.31$ and $\sigma = 1.0$ for pump X). Similarly to non-cavitating conditions, the mesh sensitivity is carried out with the sliding mesh approach, but it remains valid also for the other ones. The first employed mesh is the one already selected for the single-phase simulations. Then, the mesh is gradually refined until the performance factor converges to a stable value. The results of this procedure are shown in Fig. 18(a). It can be noted that the mesh independency is reached for a grid of 3.8 million cells, which is almost five times heavier than the one required for the single-phase simulations. Indeed, to accurately capture the vapor cavities, especially on the suction side of the blades, the number of prism layers is increased from three to ten, moving to a low Reynolds approach. For the same reason, also the bulk polyhedral mesh is refined.

Interestingly, in the present analysis, thanks to the experimental data, the conditions presenting cavitation (thus eligible to run a mesh sensitivity) are a priori known. Without experiments, it would be hard to guess the combination of flow coefficient and cavitation number that give rise to cavitation. Therefore, in that case it would be necessary to simulate a complete head loss curve, with the initial mesh and for a flow coefficient of interest, to estimate a reasonable range where cavitation can happen. Then, the mesh sensitivity analysis can be conducted for a value inside that range.

As a proof of the fact that the original mesh (for non-cavitating conditions) is not able to properly simulate cavitating operating points, a comparison in terms of head loss curve is proposed in Fig. 18 (b). The results provided by the grids selected for cavitating and non-cavitating conditions are compared. For very high CNs (i.e. cavitation is absent), the grids provide very close results. When the phenomenon manifests at low CNs, the PF values provided by the finer grid are close to the experiments while the original mesh fails to reproduce the experimental behavior of the turbomachine.

As a final comment, it is useful to point out that, for pump Y, the mesh adopted for cavitating and non-cavitating conditions is the same. Indeed, by applying refinements similar to those used on pump X, the number of cells of pump Y raises from 2.6 to 6.3 million. Simulating the

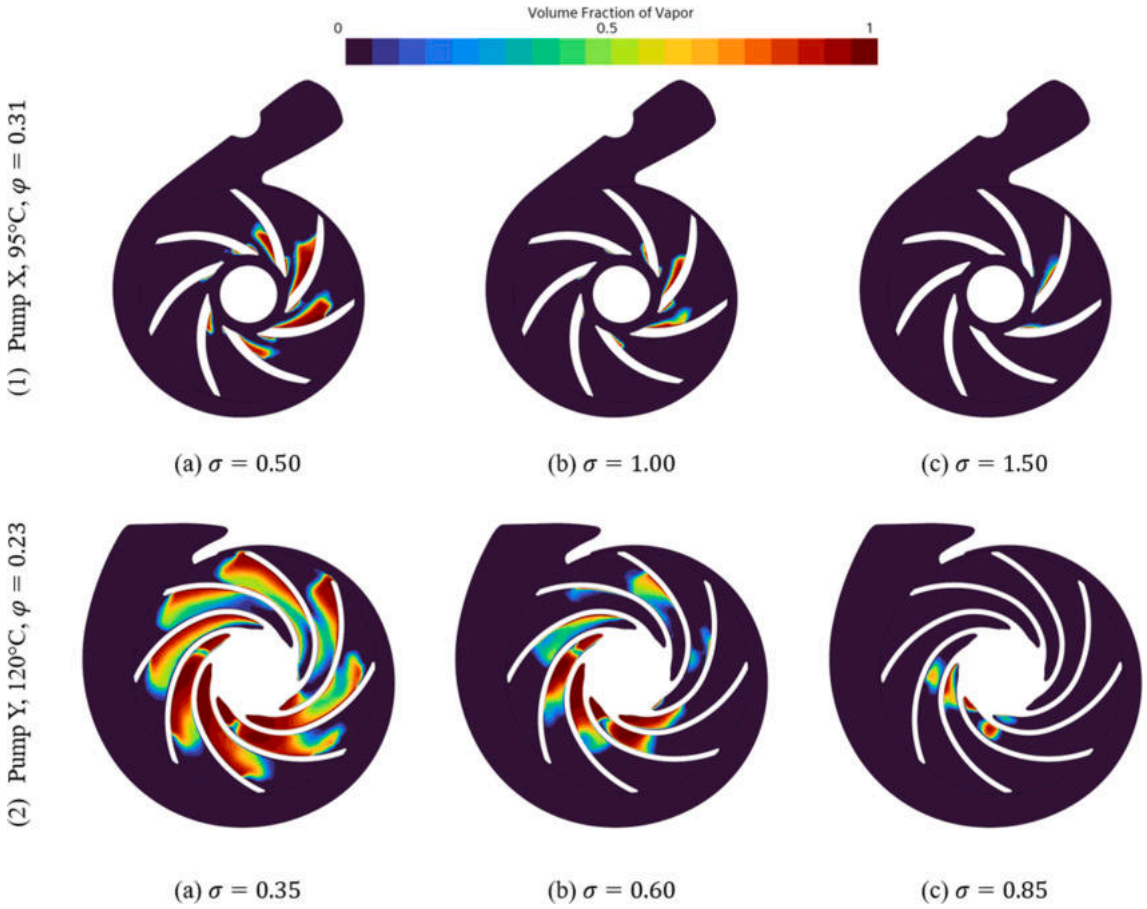

Fig. 17. Volume fraction of vapor on pump X (95 °C, $\varphi = 0.31$) and pump Y (120 °C, $\varphi = 0.23$), for different cavitation numbers, using the multi-phase sliding mesh approach.

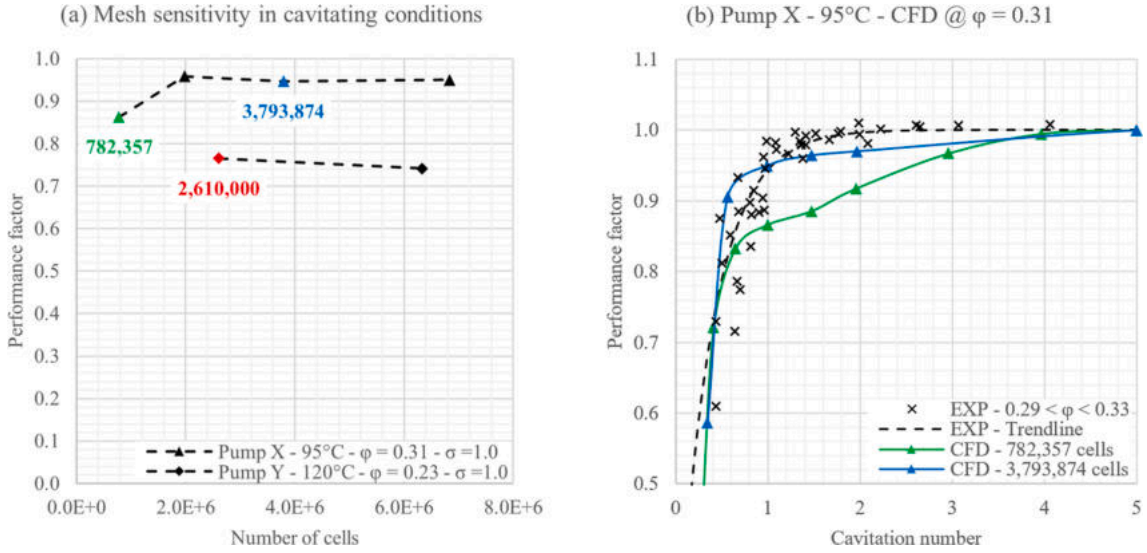

Fig. 18. (a) Mesh sensitivity for pump X (95 °C, $\varphi = 0.31$, $\sigma = 1.0$) and pump Y (120 °C, $\varphi = 0.23$, $\sigma = 1.0$) in cavitating conditions. (b) Comparison between the PF curve obtained with the initial mesh of 782,357 cells (which is suitable for non-cavitating conditions) and the improved PF curve obtained with the selected mesh of 3,793,874 cells, for pump X (95 °C, $\varphi = 0.31$).

cavitating condition at $\varphi = 0.23$ and $\sigma = 1.0$, the PF changes from 0.76 to 0.74 (Fig. 18(a)), which is a minimal variation considering that PF curves are steep at low PFs. The original mesh of pump Y is already accurate enough because of the complex geometry, which requires a fine mesh also without cavitation. Therefore, when the phenomenon occurs, the quality of the numerical grid is already sufficient to obtain mesh-independent results.

4. Conclusions

This study analyses performance and cavitation of two centrifugal pumps, which are adopted in cooling circuits of high-performance cars. This particular application is challenging mainly for two reasons.

Firstly, the increasing number of components inside a vehicle (e.g. hybrid cars) demands for more strict packaging constraints. Therefore, an automotive pump must be compact, and the shape of its ducts is mainly driven by other components of the system. As a pump gets smaller, the impeller must rotate faster to maintain the same head, increasing the likelihood of a cavitating behavior. Moreover, complex shapes of the ducts (e.g. especially pipe bends) may further disrupt the flow, reducing performance and worsening cavitation.

The second challenge lies in the vast range of operating conditions that a pump has to face in an automotive cooling circuit. A vehicle is a dynamic system whose operation greatly influences the fluid temperatures, rotational velocities, and flow rates in the pump. Consequently, an automotive pump has to be designed to deliver the required performance over a wide range of conditions and in a reliable way, i.e. minimizing cavitation.

The main goal of this study is the development of a predictive 3D-CFD methodology for the simulation of centrifugal pumps used in high-performance cooling circuits. Anyway, the results may be extended beyond the automotive field to any application where compactness, reliability, and high-performance are required. Considering the large number of modelling techniques used in literature, the methodology of this study is defined by comparing both consolidated and less common approaches. In particular, the analysis compares different turbulence models, namely k-ω SST, Realizable k-ε models, and Reynolds Stress Transport Elliptic Blending, and different rotational approaches, i.e. frozen rotor, sliding mesh and mixing plane.

The methodology is validated against experimental data from both the analysed pumps, which have similar dimensions but significantly different designs. However, the experimental data come from tests that were not intended for CFD methodology validation, but rather for the characterization of both pumps over their full ranges of operating rotational velocities and flow rates. As a consequence, a dedicated post-processing technique is developed to make the experimental data suitable for comparison with the CFD results.

The experimental and numerical investigations lead to the following conclusions:

- Employing the similitude theory of turbomachinery, a Performance Factor *PF* is defined. Through this novel parameter, it is possible to gather data on cavitation even though the experimental procedure does not rely on pump inlet pressure variations. As main output, two PF maps are generated (i.e. the value of PF for all possible combinations of flow coefficients φ and cavitation numbers σ is obtained). They show that pump X manifests cavitation for $\sigma < 0.5$, at $\varphi = 0.20$ and 95 °C, and it occurs for higher values of σ as φ increase (i.e. it is detected for $\sigma < 1.2$ at the highest value of φ). Instead, pump Y is not affected by cavitation when the fluid temperature is 100 °C. However, increasing the temperature to 120 °C, cavitation is present for $\sigma < 0.8$ in the range $0.21 < \varphi < 0.24$. In general, pump X is more performant than pump Y (i.e. higher head coefficients) but it is also more affected by cavitation, which is present at high flow coefficients for both pumps.
- Thanks to the PF, it is also possible to decouple performance analysis (i.e. head coefficient as a function of flow coefficient for sufficiently high values of cavitation number) and cavitation analysis (i.e. performance factor as a function of cavitation number for narrow ranges of flow coefficients). Therefore, turbulence models and rotational approaches are tested for the evaluation of both performance and cavitation.
- As for the ability of turbulence models to predict performance, the Realizable k-ε model shows an average deviation from experimental data of 5.5 % on pump X and 6.3 % on pump Y, while the k-ω SST deviates of 4.3 % on pump X and 3.0 % on pump Y. The more advanced RST-EB model requires about 70 % more computational time compared to the other models and it reduces the average deviation from experimental data to 2.9 % on pump X. However, the RST-EB is highly unstable on pump Y, requiring smaller time-steps and, thus, increasing the computational time of one order of magnitude. For this reason, it is excluded from further analysis. Moving to cavitation, the remaining k-ω SST and Realizable k-ε turbulence models provide similar results and are both in strong agreement with the experiments. Therefore, given the excellent balance between accuracy and computational cost, the k-ω SST model is the preferred choice for CFD simulations of automotive centrifugal pumps.
- As for the rotational approaches, the mixing plane shows an average deviation from performance experimental data of 6.8 % on pump X and 7.5 % on pump Y. Similarly, the frozen rotor deviates of 6.5 % on pump X, but it is less accurate on pump Y with a 12.2 % of deviation. Finally, the sliding mesh approach is the most accurate method (4.3 % deviation on pump X and 3.0 % on pump Y) for simulating centrifugal pump performance in non-cavitating conditions. Mixing plane and frozen rotor lose accuracy especially in off-design conditions, where they fail to capture the complex flow structures. Nevertheless, frozen rotor and mixing plane provide reasonable accuracy when employed for the design conditions. In cavitating conditions, mixing plane and frozen rotor tend to underestimate the head loss of pump X and completely fail to capture it on pump Y, even though vapor cavities are generated by the cavitation model. The sliding mesh method, instead, provides accurate results. Therefore, the sliding mesh is the preferred choice for this application, even though its computational cost is roughly an order of magnitude higher than the steady approaches.
- It must be pointed out that, in cavitating conditions, the mesh may need to be refined compared to non-cavitating ones, to allow the Volume of Fluid method to properly capture the effect of vapor formation and condensation on the pump performance. Therefore, it is necessary to carry out a more detailed mesh sensitivity analysis, to evaluate the grid both in cavitating and non-cavitating conditions. It results that one of the pumps (i.e. pump X) requires a mesh five times finer than the one used for non-cavitating conditions to correctly capture the performance loss.

The validated CFD framework offers a robust and predictive tool for the design and optimization of compact centrifugal pumps to be adopted in automotive cooling circuits, where packaging constraints, thermal variability, and reliability are critical. The results enable engineers to simulate a wide range of real driving conditions, reducing the need for expensive and time-consuming prototype testing. This accelerates the design cycles and supports the early identification of cavitation risks in hybrid and electric vehicle cooling systems. Moreover, the methodology can be readily applied to aerospace thermal management systems, battery and electronics cooling systems, and industrial compact pump systems, where high head, limited space, and reliability are essential. The findings provide quantitative guidance on turbulence model selection, mesh refinement strategies, rotational modelling approaches, and post-processing techniques, thus potentially defining future CFD best practices and development workflows.

CRediT authorship contribution statement

Ilario Cordisco: Writing – original draft, Visualization, Methodology, Investigation, Formal analysis, Data curation, Conceptualization. **Fabio Berni:** Writing – review & editing, Supervision, Methodology, Investigation. **Giovanni Paini:** Supervision, Data curation, Conceptualization. **Roberto Tonelli:** Supervision, Resources, Project administration, Funding acquisition. **Stefano Fontanesi:** Writing – review &

editing, Supervision, Software, Project administration.

Declaration of competing interest

The authors declare that they have no known competing financial interests or personal relationships that could have appeared to influence the work reported in this paper.

Data availability

The data that has been used is confidential.

References

[1] X. Zheng, W. Wang, P. Zhang, Y. Pu, Y. Zhao, Internal flow characteristics of centrifugal pumps under different startup combination schemes, Water (Basel) 16 (8) (2024), https://doi.org/10.3390/w16081087.

[2] J. Hu, K. Li, W. Su, X. Zhao, Numerical simulation of drilling fluid flow in centrifugal pumps, Water (Basel) 15 (5) (2023), https://doi.org/10.3390/w15050992.

[3] M. Siddique, S. Bellary, A. Samad, J.-H. Kim, Y.-S. Choi, Experimental and numerical investigation of the performance of a centrifugal pump when pumping water and light crude oil, Arab. J. Sci. Eng. 42 (2017) 4605–4615, https://doi.org/10.1007/S13369-017-2592-1.

[4] R. Tarodiya, B. Gandhi, Hydraulic performance and erosive wear of centrifugal slurry pumps–a review, Powder Technol. 305 (2017) 27–38, https://doi.org/10.1016/J.POWTEC.2016.09.048.

[5] A. Nemdili, D. Hellmann, The requirements to successful centrifugal pump application for desalination and power plant processes, Desalination 126 (1999) 199–205, https://doi.org/10.1016/S0011-9164(99)00175-7.

[6] S. Barbarelli, M. Amelio, G. Florio, Predictive model estimating the performances of centrifugal pumps used as turbines, Energy 107 (2016) 103–121, https://doi.org/10.1016/J.ENERGY.2016.03.122.

[7] M.L.M. Tasuni, Z.A. Latiff, H. Nasution, M.R.M. Perang, H.M. Jamil, M.N. Misseri, Performance of a water pump in an automotive engine cooling system, Jurnal Teknologi (Sci. Eng.) 78 (10–2) (2016), https://doi.org/10.11113/jt.v78.9667.

[8] L. Mariani, et al., Model based design, prototyping and testing of a small size high speed electrically driven centrifugal pump, SAE Int. J. Adv. Curr. Pract. Mobil. 5 (2022–37–0025) (2022) 967–976, https://doi.org/10.4271/2022-37-0025.

[9] X. Shao, W. Zhao, Liquid hydrogen centrifugal pump optimization based on reducing hydraulic loss and improving cavitation, Int. J. Hydrogen Energy 49 (2024) 1419–1431, https://doi.org/10.1016/j.ijhydene.2023.08.265.

[10] Q. Liu, et al., Investigation of cavitation characteristics in an aircraft centrifugal fuel pump, Flow Meas. Instrum. 96 (2024), https://doi.org/10.1016/j.flowmeasinst.2024.102521.

[11] A.A. Dehghan, M.H. Shojaeefard, M. Roshanaei, Exploring a new criterion to determine the onset of cavitation in centrifugal pumps from energy-saving standpoint; experimental and numerical investigation, Energy 293 (2024), https://doi.org/10.1016/j.energy.2024.130681.

[12] P. Song, Z. Wei, H. Zhen, M. Liu, J. Ren, Effects of pre-whirl and blade profile on the hydraulic and cavitation performance of a centrifugal pump, Int. J. Multiph. Flow 157 (2022), https://doi.org/10.1016/j.ijmultiphaseflow.2022.104261.

[13] R. Ramirez, E. Avila, L. Lopez, A. Bula, J. Duarte Forero, CFD characterization and optimization of the cavitation phenomenon in dredging centrifugal pumps, Alexandria Eng. J. 59 (1) (2020) 291–309, https://doi.org/10.1016/j.aej.2019.12.041.

[14] G. Li, et al., Liquid-vapor two-phase flow in centrifugal pump: cavitation, mass transfer, and impeller structure optimization, Vacuum 201 (2022), https://doi.org/10.1016/j.vacuum.2022.111102.

[15] X. Li, S. Yuan, Z. Pan, J. Yuan, Y. Fu, Numerical simulation of leading edge cavitation within the whole flow passage of a centrifugal pump, Sci. China Technol. Sci. 56 (9) (2013) 2156–2162, https://doi.org/10.1007/s11431-013-5311-5.

[16] R. Tao, R. Xiao, F. Wang, W. Liu, Cavitation behavior study in the pump mode of a reversible pump-turbine, Renew. Energy 125 (2018) 655–667, https://doi.org/10.1016/j.renene.2018.02.114.

[17] X. Wang, Y. Wang, H. Liu, Y. Xiao, L. Jiang, M. Li, A numerical investigation on energy characteristics of centrifugal pump for cavitation flow using entropy production theory, Int. J. Heat Mass Transf. 201 (2023), https://doi.org/10.1016/j.ijheatmasstransfer.2022.123591.

[18] G. Li, et al., Deep learning, numerical, and experimental methods to reveal hydrodynamics performance and cavitation development in centrifugal pump, Expert Syst. Appl. 237 (2024), https://doi.org/10.1016/j.eswa.2023.121604.

[19] H. Zhang, et al., Analysis the composition of hydraulic radial force on centrifugal pump impeller: a data-centric approach based on CFD datasets, Appl. Sci. (Switzerland) 15 (13) (2025), https://doi.org/10.3390/app15137597.

[20] A. Nycz, J. Skrzypacz, P. Szulc, Influence of gap blade geometry on the energy performance of low-specific-speed centrifugal pumps, Energies (Basel) 18 (11) (2025), https://doi.org/10.3390/en18112867.

[21] Y. Nishi, K. Konno, S. Ono, Multi-objective optimization design method for single-blade centrifugal pump impellers to improve performance and reduce radial thrust, Eur. J. Mech. B/fluids 114 (2025), https://doi.org/10.1016/j.euromechflu.2025.204311.

[22] O. Dumitrescu, C. Dobromirescu, V. Dragan, I.S. Vintila, R. Mihalache, CFD and experimental comparison for micro-pump performance in space applications: a case study, Appl. Sci. (Switzerland) 15 (12) (2025), https://doi.org/10.3390/app15126623.

[23] T. Huang, T. Wang, Q. Guo, P. Shu, Q. Gou, Energy loss analysis of a multi-stage centrifugal pump using in pump mode and turbine mode, Energy 334 (2025), https://doi.org/10.1016/j.energy.2025.137784.

[24] C.E. Brennen, Hydrodynamics of Pumps, Cambridge University Press, Cambridge, 2011, 10.1017/CBO9780511976728.

[25] Siemens digital industries software, “Simcenter STAR-CCM+,” (2022) 2210.1.

[26] A. Mohan, G. Tomar, Volume of Fluid Method: A Brief Review, Springer, 2024, 10.1007/s41745-024-00424-w.

[27] J. Sauer, G. Schnerr, Unsteady cavitating flow - a new cavitation model based on a modified front capturing method and bubble dynamics, Proc. 2000 ASME Fluid Eng. Summer Conf. 251 (2000) 1073–1079.

[28] T.-H. Shih, W.W. Liou, A. Shabbir, Z. Yang, J. Zhu, A new k-epsilon viscosity model for high Reynolds number turbulent flows, (1995). doi: 10.1016/0045-7930(94)00032-T.

[29] F.R. Menter, Two-equation eddy-viscosity turbulence models for engineering applications, AIAA J. 32 (8) (1994) 1598–1605, https://doi.org/10.2514/3.12149.

[30] R. Manceau, K. Hanjalić, Elliptic blending model: a new near-wall Reynolds-stress turbulence closure, Phys. Fluids 14 (2) (2002) 744–754, https://doi.org/10.1063/1.1432693.

[31] S. Lardeau, R. Manceau, Computations of complex flow configurations using a modified elliptic-blending Reynolds-Stress model, in: 10th International ERCOFTAC Symposium on Engineering Turbulence Modelling and Measurements, Marbella, Spain, (2014). [Online]. Available: https://hal.science/hal-01051799v1.

[32] J.F. Gülich, Centrifugal pumps, second ed., Springer, Berlin, Heidelberg, 2010, 10.1007/978-3-642-12824-0.